Instituto Tecnológico y de Estudios Superiores de Monterrey

Campus Monterrey

School of Engineering and Sciences

Simulation of a centrifugal microfluidic device for particle separation through acoustophoresis

A thesis presented by

Montserrat Rubio Téllez

Submitted to the
School of Engineering and Sciences
in partial fulfillment of the requirements for the degree of

Master of Science

In

Nanotechnology

Monterrey Nuevo León, August 2nd, 2021

Dedication

To my family who have always supported me.

Acknowledgements

I would like to thank my advisors Dr. Sergio Omar Martínez Chapa and Dr. Masoud Madadelahi for guiding me through this project. Dr. Mallar Ray for all his suggestions and comments on the thesis report, and for being an excellent professor.

Thanks to my family, for all the support and love they always give me. This couple of years made me really appreciate it.

Thanks to my friends, who were always there. Thanks to Rodrigo, for all his support and motivation this last year, and for making my stay in Monterrey the best of it.

I am grateful to Tecnológico de Monterrey, for the tuition scholarship, and for being my second home 9 years of my life. I will always be proud to have belonged to this institution.

And finally, thanks to CONACYT for the scholarship during my master studies.

Simulation of a centrifugal microfluidic device for particle separation through acoustophoresis

By
Montserrat Rubio Téllez

Abstract

Particle and cell separation is a fundamental operation in biomedical research and clinical diagnostics. Circulating tumor cells (CTCs) separation is gaining interest because its detection and further study can help in early cancer diagnosis or provide guidance in chemotherapy treatment. Acoustophoresis in microfluidic devices has the potential to separate CTCs and rare cells from blood samples. This technology manipulates particles with acoustic waves and is a contact-free, label-free and highly sensitive technique. There has not been any experimental or computational study integrating acoustophoresis in centrifugal microfluidic platforms. This work presents the proof of concept of both principles for particle and cell separation, through the simulation of the device. A 3D FEM-based model was built in COMSOL for predicting the particles path. The geometry consisted first in a Surface Acoustic Wave based device with 2 pairs of IDTs located on top of a piezoelectric substrate, with a rectangular fluid channel with three inlets and three outlets. By applying boundary conditions, input parameters, and considering centrifugal, Coriolis, drag, lift and acoustic radiation forces; the particle's paths are obtained. An attempt to validate the model with a previous experimental work was not successful since the acoustic pressure field was not generated correctly. However, the model was validated with a previous published simulation work of a non-centrifugal platform, and then used for computational demonstration of acoustophoretic separation of CTCs from white blood cells and red blood cells. A parametric analysis was performed to study the influence of five parameters on the efficiency of the device. Results showed that the recovery rate of CTCs at the center-outlet decreases when the angular velocity increases, when the distance to the axis of rotation increases, and when the distance between the IDTs and the channel increases. Recovery rate of CTCs at the center-outlet increases when voltage increases. Centrifugal platforms were found to be more sensitive to density variations. The model was modified to simulate a Bulk Acoustic Wave-based device and an attempt to validate it with a previous experimental work was done, however limitations were found. This work provides an understanding of the behavior of a centrifugal microfluidic platform with acoustophoresis and might be used as the initial reference for future computational work for correctly generating the acoustic pressure field and subsequently future experimental studies of particle and cell separation.

List of Figures

List of Tables

Contents

Chapter 1

Introduction

The ability to sort particles into different populations based on their physical characteristics is a fundamental operation in healthcare, in the food and chemical industry, and in environmental assessments [1].

In healthcare, separation of cells is a crucial task and powerful tool in biomedical research, clinical diagnostics and cell therapy [2]. In research, the separation of cell samples is commonly the first stage for further analysis of a single type of cell or for studying the effect of drugs or treatments on specific cell populations [3]. In clinical diagnostics, blood samples are separated for the analysis of individual components and identification of diseases [4]. However, there are some types of cells known as rare cells with extremely low concentration, going from 1-100 cells per mL of blood; and conventional isolation techniques do not separate them correctly [5]. Typical rare cells in blood are circulating tumor cells (CTCs), and its separation from cancer patients' blood is gaining interest due to the important implications it may have [6].

Cancer is the second cause of death in the world, with a total of 9.6 million in 2018 [7]. When cancer spreads to a different part of the body from where it started, it is called metastasis, and metastatic spread is the major cause of death from cancer [8]. Therefore, early detection is essential for improving the survival rate, which is very challenging, especially in low and middle income countries.

A CTC is a cancer cell circulating around the body in the bloodstream after being shed from a primary tumor [9]. CTCs are believed to be the reason of additional tumors or metastases in other organs. The detection and analysis of CTCs as liquid biopsy of tumors is a powerful tool to fight against cancer since it helps in early patient diagnosis and can provide guidance in chemotherapy treatment by monitoring individual response [10].

However, because CTCs are rare cells, they must be isolated and enriched from blood samples to be effectively studied in subsequent analysis. Current technologies on the market of CTCs detection mainly use magnetic-activated and fluorescence-activated

cell sorting, such as CellSearch, the only test approved by U.S. food and drug administration (FDA) for detecting CTCs [11]. These techniques are high cost, need expertise for handling, have long detection time. have low purity of capture and require labeling with specific antibodies [11-15]. Therefore, new CTCs separation methods are required to overcome these limitations.

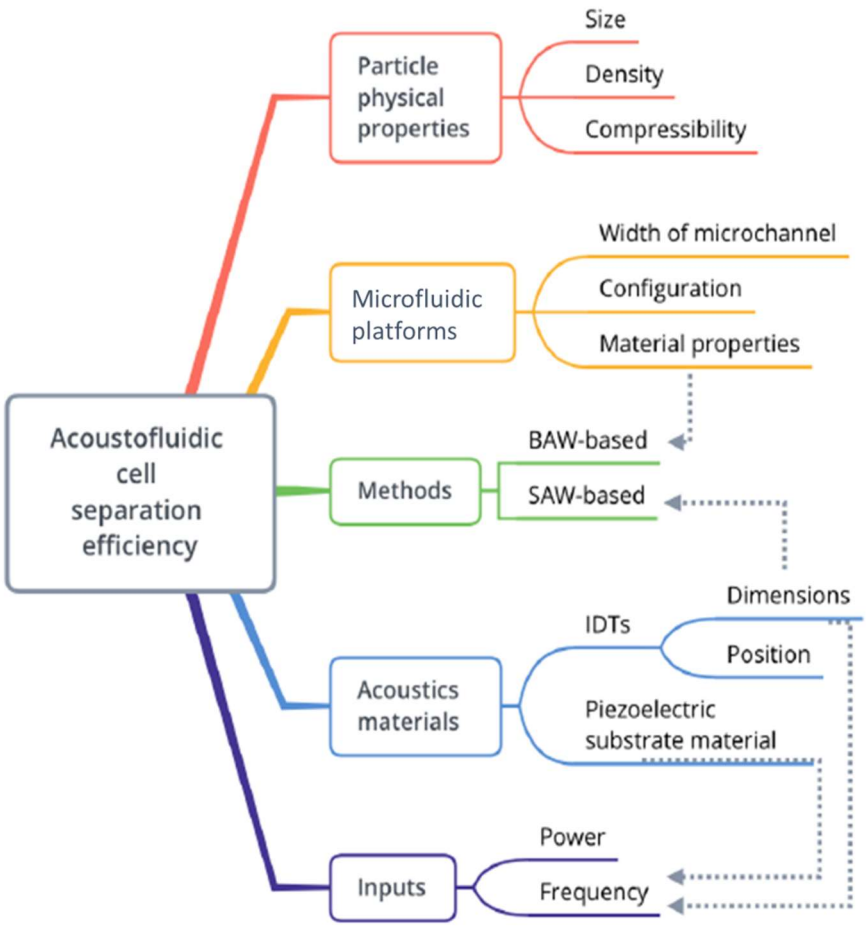

Figure 1 Factors that determine the efficiency of acoustofluidic cell separation

The technology that may have the potential to separate CTCs and rare cells in general is acoustofluidics [16]. Acoustofluidics is the combination of acoustophoresis and microfluidics, meaning that the movement of particles is caused by acoustic waves. The application of this technology is growing in recent years since it offers multiple advantages. It is a contact-free, label-free, and non-invasive method for cell manipulation, it has high biocompatibility, high sensitivity, a simple fabrication, and compatibility with other lab-on-a chip components [17]. However, research is still focused on developing

more efficient platforms for particle and rare cell separation. Figure 1 shows the multiple factors that determine the efficiency of the device. Scientists have been modifying these variables and isolating particles, cells, and CTCs from biological samples in traditional chip-based platforms [34-36].

On the other hand, centrifugal microfluidic platforms are potentially capable of becoming the standard tool for regular diagnostics [21]. They offer advantages in comparison to common chip-based microfluidic systems, such as high-performance fluid manipulation with minimal amount of instrumentation since they work with a compact motor without the need of syringe pumps [22]. Different microfluidic functions can be added on the platform, making it a promising technology for diagnostics and point-of-care applications [23].

The objective of the project is the proof of concept of acoustophoresis in centrifugal microfluidic platforms, through the design and simulation of a functional device for particle separation. There has not been any experimental study or computational simulation joining these two methods, it is a new territory to focus research. Simulation and modeling are useful techniques for predicting the performance of the microfluidic device and for finding optimal parameters before fabrication and experimentation. It also gives better understanding of the behavior of particles and flow inside the microfluidic platform. This work might be used as the initial reference for future rare cell separation through acoustophoresis in centrifugal platforms.

The thesis is organized in 6 Chapters, beginning with an Introduction to the project. Chapter 2 presents the state-of the art of particle and cell separation in microfluidics, emphasizing in platforms using acoustophoresis. Chapter 3 focuses on the theoretical background which describes the particle movement on the microfluidic platform. Chapter 4 shows the methodology used for this work, and Chapter 5 discusses the results. Finally, Chapter 6 presents the conclusions and future work of the project.

Chapter 2

State of the Art

This chapter presents a review of previous works related to particles, cells and CTCs separation using acoustophoresis in microfluidic platforms. The design of the device, the working principle, the materials used, the input parameters, and the efficiency obtained is included.

2.1 Particle and cell separation in microfluidics

Particle and cell separation through microfluidics has the benefit of being low cost, small size, and biocompatible [16]. It can be divided into passive and active techniques. Passive separation techniques use the interaction between particles, flow field and the structure of the channel to separate particles of different properties, with no need of external forces. Meanwhile, active separation techniques use external forces in different forms for sorting the particles, offering better performance [25]. Some devices use a combination of both.

Acoustic particle separation is an active technique which uses the acoustic

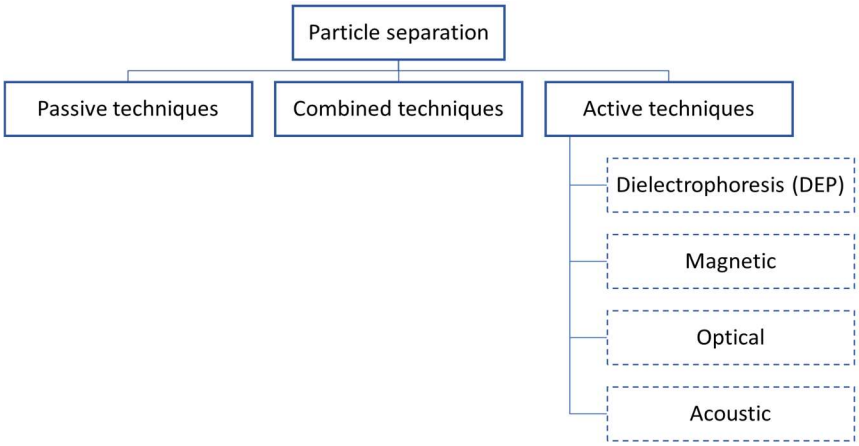

Figure 2 Particle separation techniques in microfluidics

radiation force for separating particles with different properties. Previous works using this method for particle and cell isolation are presented.

Dykes et al. [26] developed a device of platelet removal from peripheral blood which worked with bulk acoustic wave (BAW) configuration. The silicon channel had a width of 380 um, so it could match half the wavelength resonance of 2MHz. The acoustic wave was generated by a piezoelectric transducer situated at the middle of the channel, as shown in Figure 3 The recovery rate of platelets from peripheral blood cells was of 89%. Recovery rate is a parameter for measuring the efficiency of the device, and refers to the number of targeted particles collected in the outlet to the total number of those particles in the inlet

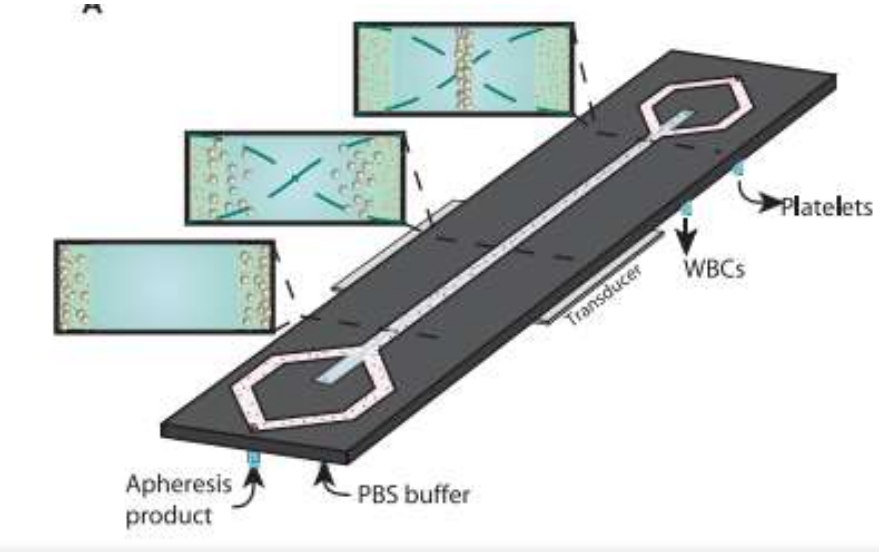

Figure 3 Schematic of the device with BAW configuration [26]

The same group of researchers improved their platform and separated prostate cancer cells from WBC using acoustophoresis [27]. A pre-alignment step was added to the device, achieving a 99% of purity while separating 5 μm and 7 μm microspheres. A recovery rate of 93.6%-97.9% and purity of 97.4% to 98.4% was achieved in cancer cell separation. The pre alignment transducer worked with 4.97 MHz and the separation transducer was set to 1.94 MHz. Some years later [28], with a similar platform, they separated neuroblastoma cells from peripheral blood mononuclear cells (PBMCs) with 60-97% of recovery rate.

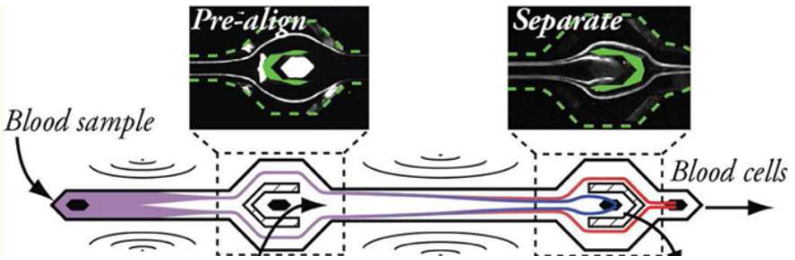

Figure 5 Schematic of the device with BAW configuration with pre-alignment section [27]

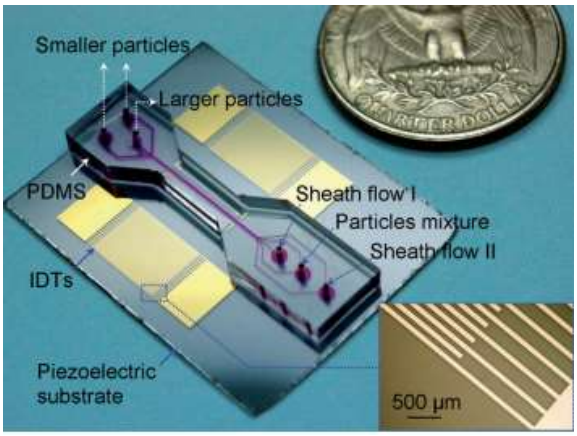

Figure 4 Image of the device consisting of a pair of IDTs, a PDMS channel with its inlets and outlets and a piezoelectric substrate [29]

Shi et al. [29] developed a particle separation method in a microfluidic channel using standing surface acoustic waves (SSAWs). Polystyrene beads with equal densities but different volumes (4.17 μm and 0.87 μm in diameter) were introduced on the two-sided inlets of the channel, DI water as sheath flow was injected in the central channel, and a SSAW was produced in the channel by two parallel IDTs. Larger particles moved to the center of the channel, where the pressure node was located. It was a simple method for separating all kind of particles disregarding polarization properties with high separation efficiency and low power consumption. BAW methods demands that the channel should be made of silicon or glass due to the necessity of acoustic reflection properties, but here, the acoustic wave was confined to the substrate, allowing the channel to be of PDMS. Furthermore, the device was fabricated using standard MEMS and soft-lithography procedures, allowing small-sized fabrication, easy integration, and making it cost-effective for mass production. The recovery rate of the developed platform was 80%, but

the efficiency and speed could be regulated by changing the power, the wavelength of the SAWs, the speed of the sample flow, and the geometry of the channel.

Nam, et al. [30] presented a similar method, in which 3 types of particles of different diameter (d_1= 1, d_5= 5 and $d_1 = 10$ μm) were continuously separated using SSAW in a microchannel. Particle mixture was introduced through the center inlet while sheath flow through the two-sided inlets. In this way, particles were hydrodynamically focused at the middle stream, represented as $w/2$ in Figure 6A, w being the width of the channel. Then, when particles entered the acoustic field, and SSAW displaced the larger particles ($d_5\ and\ d_{10}$) toward the sided wall where the nodes were generated by the 2 IDTs, as Figure 6B presents. The smaller particles (d_1) stayed mainly at the middle of the channel, where the shear rate was low. This method had the potential to be used with shear-dependent cells. However, it had a limitation with sub-microparticles (0.1-1 μm), since SSAW was not effective for manipulating them. The frequency was set to 19.5MHz.

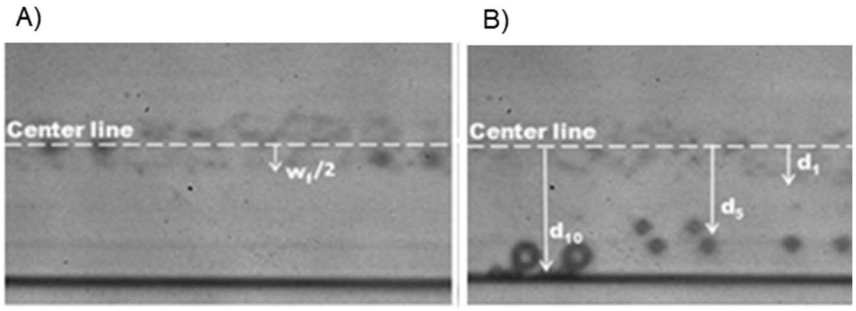

Figure 6 Images of particles of three different sizes being A) hydrodynamically focused at the centerline, and B) displaced within the SSAW field [30]

Nam, et al. [31] later developed a platform for separating beads with encapsulated cells using acoustophoresis. Beads were of equal sizes but different densities, since the number of encapsulated cells varied. As Figure 7A shows, beads with larger densities (with larger number of encapsulated cells) moved toward the sided walls, where the pressure nodes were generated. The sample flow rate was 8 uL/min and the sheath flow rate 16 uL/min. The working frequency was 3.94 MHz, and the optimum applied voltage 12V. The recovery rate reached was 97% and a purity of 98% at a rate of 2300 beads per

minute. A cell viability test showed that encapsulated cells were not damaged with the acoustic force.

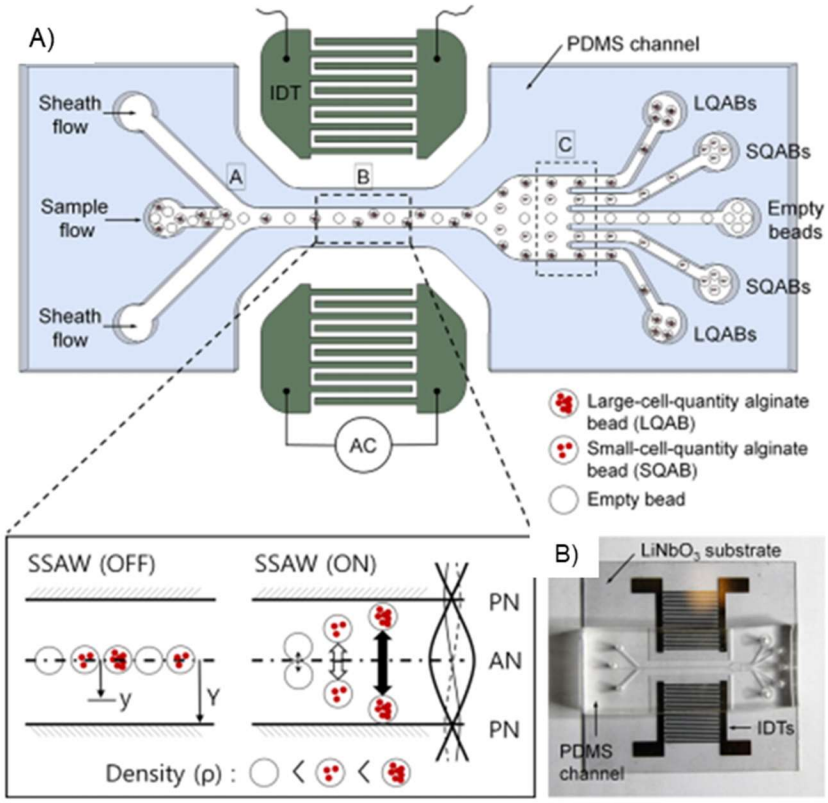

Figure 7 A) Schematic illustration of the SSAW device with the separation principle B) Photograph of the device consisting of a pair of IDTs, a PDMs channel and a piezoelectric substrate [31]

Ai et al. [32] developed a microfluidic device and through acoustophoresis separated Escherichia coli (E-coli) bacteria from peripheral blood mononuclear cells (PBMSCs) with a 95.65% of purity. These cells were different in size (1.1μm and 7.23μm in diameter). A FEM model was also presented simulating the acoustic pressure field to understand better the particle separation through SSAW. The frequency used was 12.98MHz. The cell mixture had a flow rate of 0.5 μl/min, and the sheath flow of 4 μl/mmin. This technique could be further used to diagnose bloodstream infections induced by bacteria.

Ding, et al [33] presented a different configuration to improve the efficiency and sensitivity of acoustic separation techniques. They introduced a tilted angle standing surface acoustic wave (taSSAW) platform [Figure 8A], where the pair IDTs were placed parallel with respect to each other, but at an inclined angle with respect to the channel and flow direction. Multiple pressure nodal lines were generated instead of only one, in comparison to the previous platforms. This way, particles not captured by the first pressure node could eventually be captured at the next one, and moved to the right path for collection [Figure 8B and 8C]. The angle was set to 30º, and polystyrene beads of 2 and 10 µm in diameter were separated with a recovery rate of 99%. Then, the platform showed a rate of 97% with polystyrene beads of similar size (7 and 9.9 µm in diameter). Furthermore, they separated MCF-7 human breast cancer cells from normal WBCs with a recovery rate of 71% and a purity of 84%, with no significant damage on the cells according to the viability test.

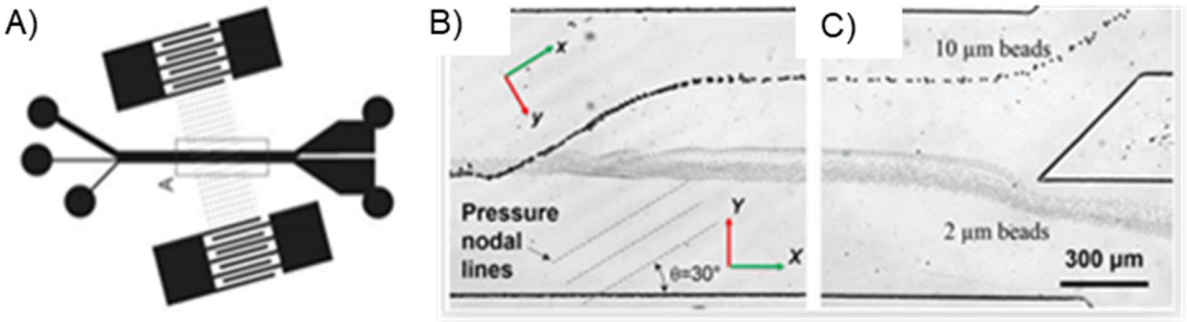

Figure 8 A) Schematic representation of the device with tilted angle B) Separation process for polystyrene beads in the taSSAW working region and C) in the outlets [33]

The same group of researchers a year later [34] separated a variety of cancer cells from cell culture lines from WBCs with the tilted-angle SSAWs method. The cancer cells used were breast cancer cells (MCF-7), cervical cancer cells (HeLa), melanoma cancer cells (UACC903M-GFP) and prostate cancer cells (LNCaP). They had average diameters between 16 and 20 µm, while the WBCs were 12 µm. The geometry of the device and the tilt angle were optimized by parametric numerical studies. With different flow rates, the optimum tilt angle would be different, 20 µL/min was defined, with an angle of 5º. The

input power was set to 35 dBm and 19.573 MHz. The cancer cell recovery rates obtained were between 83-93%. Then, the separation was performed with real clinical samples, CTCs were isolated from blood samples of patients with breast cancer. The method presented worked well with rare cells that are largely different from WBCs, but with small differences, it was expected to be less effective.

The platform was then modified [35] and isolation of rare CTCs from peripheral blood was repeated. A hybrid PDMS-glass channel was used to increase the energy density and the throughput of the device. Glass has a larger impedance, so by placing a thin glass layer at the top of the microchannel, the acoustic energy increased from 4% to 89%. This increment made the device generate larger acoustic radiation forces on cells. Furthermore, a divider at the junction of inlets was added to decrease the flow velocity of cells in the channel. With this, separation efficiency was improved because CTCs stayed more time in the acoustic field. Single CTCs and clusters of CTCs were isolated, with a recovery rate of 86%, and by preserving the cell's integrity.

Wang et al. [36] developed a multistage device with a pair of straight IDTs and a pair of focused IDTs (FIDTs) to separate tumor cells from RBCs. The straight IDTs generated standing SAWs, which placed the CTCs and RBCs at the pressure nodes. Then, the focused IDTs generated focused travelling pulsed SAWs (TSAWs) and isolated the CTCs from the blood cells. The separation was first done with 2μm and 5μm polystyrene particles with a recovery rate of 94.2%. Then, U87 glioma cells were isolated from RBCs with the rate of 90%. The device relied entirely on the acoustic waves for focusing, it did not use sheath flow like previous methods, so there was no sample dilution. The TSAW separation seemed to be more robust because the acoustic radiation force is more sensitive to the size of particles in comparison to SAW method. Besides, because of the short duration of the pulses, the integrity of the cells is better kept. The flow rate of the sample was 0.3 μL/min, and the frequency in particle separation was of 29.78 MHz for IDTs, and 38.79 MHz for FIDTs.

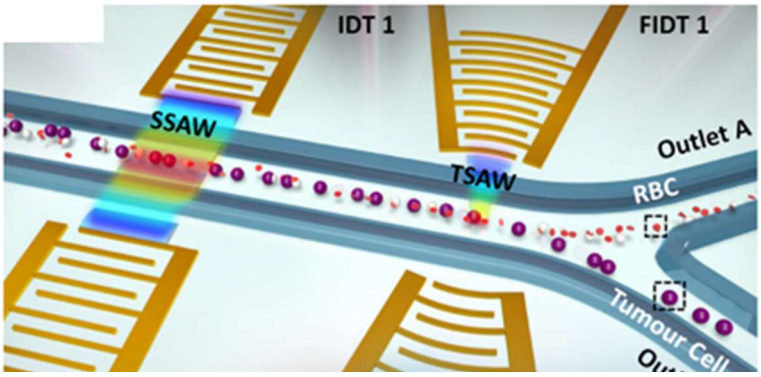

Figure 9 Schematic representation of the device with focused IDTs [36]

SAW-based devices have the advantage over BAW-devices of not having geometrical and material restrictions. Table 1 summarizes experimental works of particle and cell separation through acoustophoresis using SAWs.

Besides experimental studies, there have been some efforts to understand and optimize SAWs devices by numerical methods. Shamloo et al. [54] presented a finite element simulation of acoustic separation of blood components using SAWs in a rectangular channel. The model calculated the acoustic pressure within the channel and cell trajectories were obtained in 2D by solving the equations of motion. They presented another similar work but with a trapezoidal channel instead [55] for making more efficient the separation. A parametric study with the input voltage and the flow rate was performed to optimize the device.

Table 1 Particle and cell separation in microfluidics through acoustophoresis

Application	Acoustic wave	Addition	Particle diameter	Frequency	Flow rate	Recovery rate	Author
Size-dependent particle separation	SAW	-	4.17, 0.87 μm	12.6MHz	0.6–2 μL/min	80%	Shi et al. [29]
Size-dependent particle separation	SAW	-	1, 5, 10 μm	19.5MHz	0.03, 0.1, 0.3 μL/min	99%	Nam et al. [30]
Density-dependent particle separation	SAW	-	-	3.94MHz	sample 8 μL/min, sheath flow 16uL/min	97%	Nam et al. [31]
E-coli Bacteria separation from PBMCs	SAW	-	1.1 and 7.23 μm	12.98MHz	sample 0.5 uL/min,	95.65%	Ai et al. [32]

					sheath flow 4μL/min.		
Size-dependent particle separation and MCF-7 from WBCs	SAW	tilted angle	2 and 10 μm 7.3 and 9.9 μm	19.4MHz	-	99%, 97%, 71%	Ding et al. [33]
Cancer cells from WBCs	SAW	tilted angle	cancer cells 16-20 μm and WBCs 12 μm	19.573 MHz	20 μL/min	83-93%	Ding et al. [34]
CTCs from peripheral blood	SAW	hybrid PDMS-glass channel, a divider, tilted angle	-	19.9 MHz	-	86%	Wu, et al. [35]

Size-dependent particle separation and CTCs from RBCs	SAW	2 stages: IDTs and FIDTs	-	29.78 MHz or IDTs, and 38.79 MHz for FIDTs	0.3	μL/min	94.2% in particles. 90% in cells	Wang et al. [36]

Chapter 3

Theoretical Background

This chapter presents the working principle behind microfluidics, centrifugal platforms, and acoustophoresis.

3.1 Microfluidics

Microfluidics is the branch of fluid mechanics which studies the flow and manipulation of fluids in sub-millimeter sized channels. At this scale, viscosity dominates over inertia [37], so laminar flow rather than turbulence governs the behavior of the fluid, making it predictable and with outstanding control. One of the main applications of microfluidics is known as Lab-on-a-chip (LOC) technology which integrates one or several laboratory procedures in a small device and reduces laboratory workspace, sample and reagent volumes, while enhancing efficiency of processes [38].

The Reynolds number is a dimensionless parameter which helps in predicting the behavior of fluid flow. It is defined as the ratio of inertial force to viscous force [39]:

$$Re = \frac{F_{inertia}}{F_{viscous}} = \frac{\rho_f V_{avg} D_h}{\mu_f} \tag{3.1}$$

where ρ_f is the density of the fluid, $V_{avg}$is the average velocity of fluid flow, D_h the characteristic length or hydraulic diameter of the channel, and μ_f the dynamic viscosity. Microfluidics tends to have low Reynolds numbers [43], so the devices operate with laminar flow rather than turbulent flow inside their channels, characterized by a smooth and continuous fluid motion.

The governing equations in microfluidics [40] are the Navier-Stokes equations for momentum conservation (Equation. 3.2) and the continuity equation for mass conservation (Equation. 3.3):

$$\rho_f \frac{\partial \vec{V}_f}{\partial t} + \rho_f\left(\vec{V}_f \cdot \nabla \vec{V}_f\right) = -\nabla p + \mu_f \nabla^2 \vec{V}_f + \rho_f \vec{g} + \vec{f}_b \tag{3.2}$$

$$\frac{\partial \rho_f}{\partial t} + \nabla \cdot \left(\rho_f \vec{V}_f\right) = 0 \tag{3.3}$$

where $\vec{V}_f$ is the velocity vector of the fluid, p the pressure, and $\vec{f}_b$ the sum of all body forces.

3.2 Centrifugal microfluidic platforms

Centrifugal microfluidic platforms, commonly known as lab-on-a-disc (LOD); achieve the manipulation of samples and reagents by the rotation of the platform. Advantages of LODs over LOCs are the minimal amount of instrumentation needed to manipulate the fluid, the capacity to handle a wide range of fluid flow rate, which goes from $10\ nL/s$ to $100\ \mu L/s$ [41]; the opportunity to integrate multiple operations in a single disc [42], the removal of bubbles and residual liquids, and the possibility to analyze different types of samples regarding pH, ionic strength, or its chemical composition [40].

Physics behind centrifugal microfluidic platforms is described by 3 forces [40]: the Centrifugal force (Equation. 3.4), the Coriolis force (Equation. 3.5), and the Euler force (Equation. 3.6).

$$\vec{f}_{centrifugal} = -\rho_f \vec{\omega} \times (\vec{\omega} \times \vec{r}) \tag{3.4}$$

$$f_{Coriolis} = -2\rho_f \vec{\omega} \times \vec{V}_f \tag{3.5}$$

$$\vec{f}_{Euler} = -\rho_f \frac{d\vec{\omega}}{dt} \times \vec{r} \tag{3.6}$$

where $\vec{\omega}$ refers to the rotational velocity vector and $\vec{r}$ to the radial position vector. The forces are expressed per unit volume.

From the standpoint of physics, centrifugal force is the pseudo force arising due to accelerated motion. It is directed radially outward the disc and is the main force providing movement to the liquid. The Coriolis force, which becomes important with high angular frequency, acts perpendicular to the linear velocity and angular velocity vector. The Euler force is proportional to the angular acceleration and depends on its direction, so when the device rotates at constant angular velocities, it becomes zero. These three forces are represented in Figure 10.

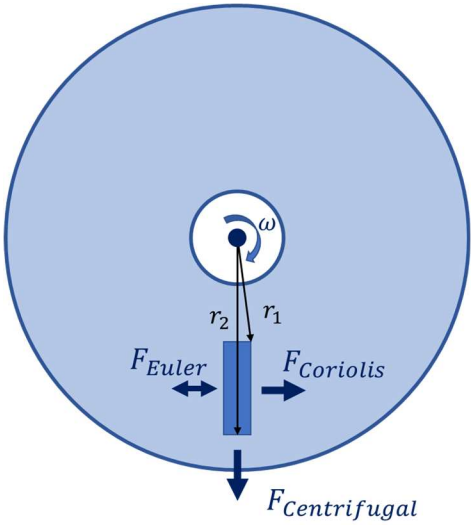

Figure 10 Forces acting on a centrifugal microfluidic platform

The addition of the three forces are the body forces $\vec{f}_b$ from Equation. 3.2. on a rotating platform.

$$\vec{f}_b = \vec{f}_{centrifugal} + \vec{f}_{Coriolis} + \vec{f}_{Euler} \tag{3.7}$$

$$\vec{f}_b = -\rho_f \vec{\omega} \times (\vec{\omega} \times \vec{r}) - 2\rho_f \vec{\omega} \times \overrightarrow{V_f} - \rho_f \frac{d\vec{\omega}}{dt} \times \vec{r}$$

The vectorial forces can also be expressed in scalar differential pressures. The centrifugal pressure difference Δp between the inner and outer points of a radial channel filled with fluid can be calculated with Equation. 3.8 [42]:

$$\Delta p = \frac{1}{2}\rho_f \omega^2 (r_2^2 - r_1^2) = \rho_f w^2 \bar{r} \Delta r \tag{3.8}$$

where r_1 is the inner radial point of the fluid column seen in Figure 10, and r_2 the outer radial point. $\Delta r = |r_2 - r_1|$ is the length of the fluid column, meaning the difference between r_1 and r_2. $\bar{r} = \frac{(r_2 + r_1)}{2}$ is the average distance of points r_1 and r_2

For tracking the particles in the microchannel, Newton's law of motion is used [40]

$$m_p \frac{d\vec{V}_p}{dt} = \sum \vec{F} \tag{3.9}$$

where m_p is the mass of the particle, $\vec{V}_p$ the velocity vector of the particle, and $\vec{F}$ the force vector affecting the particles.

The forces applied to particles due to rotation of the platform in LOD devices are the centrifugal, Coriolis and Euler forces, as mentioned previously. Equation. 3.8 becomes:

$$m_p \frac{d\vec{V}_p}{dt} = \vec{F}_{centrifugal} + \vec{F}_{Coriolis} + \vec{F}_{Euler} \tag{3.10}$$

Considering a sphere particle with mass m_p, moving with a velocity $\vec{V}_p$ at a distance r from the center of rotation, the forces are defined as [43]:

$$\vec{F}_{centrifugal} = -m_p \vec{\omega} \times (\vec{\omega} \times \vec{r}) = -(\rho_p - \rho_f) \frac{\pi d_p^3}{6} \vec{\omega} \times (\vec{\omega} \times \vec{r}) \tag{3.11}$$

$$\vec{F}_{Coriolis} = 2m_p \vec{\omega} \times \vec{V}_p = -2(\rho_p - \rho_f) \frac{\pi d_p^3}{3} \vec{\omega} \times \vec{V}_p \tag{3.12}$$

$$\vec{F}_{Euler} = -m_p \frac{d\vec{\omega}}{dt} \times \vec{r} = -(\rho_p - \rho_f) \frac{\pi d_p^3}{6} \frac{d\vec{\omega}}{dt} \times \vec{r} \tag{3.13}$$

where ρ_p is the density of the particle. Because the particles are submerged in liquid, the buoyancy is considered, so $(\rho_p - \rho_f)$ is used instead of ρ_p.

Besides the forces due to rotation of the platform, additional forces may be acting on the particles:

$$m_p \frac{d\vec{V}_p}{dt} = \vec{F}_{centrifugal} + \vec{F}_{Coriolis} + \vec{F}_{Euler} + \vec{F}_{Drag} + \vec{F}_{Lift} + \vec{F}_{External} \tag{3.14}$$

The drag force acts opposite to the relative motion of the particle with respect to the surrounding fluid, parallel to the flow direction. For the case of small spherical particles moving slowly in a viscous fluid (very low Reynolds number, $10^{-4} < Re' < 0.2$) the Stokes' drag is used [44]:

$$\vec{F}_{Drag} = 3\pi\mu d_p(\vec{V}_f - \vec{V_p}) \tag{3.15}$$

The lift forces act perpendicular to the flow direction. There are different types of lift forces to which the particle can be subjected on centrifugal microfluidics [40, 45]. The Saffman lift force is generated due to the pressure difference on two sides of the particle. Considering a spherical particle, it is expressed as:

$$\vec{F}_{Saffman} = k{d_p}^2(\vec{V}_f - \vec{V}_p)(\mu_f \rho_f \beta)^{1/2} \quad (3.16)$$

where β is the shear rate, and k a constant with value $k = 1.615$.

The Wall-induced lift force is generated due to the channel walls creating a velocity gradient of fluid around the particle. Considering a spherical particle, it is expressed as [24,43]:

$$\vec{F}_{wall-induced} = \frac{\rho_f {r_p}^6}{{D_h}^2}\left(\hat{\beta}^2 G_1(s) + \hat{\beta}\hat{\gamma} G_2(s)\right)\vec{n} \quad (3.17)$$

where r_p is the radius of the particle, $\hat{\beta}$ the dimensionless shear rate, $\hat{\gamma}$ the dimensionless shear gradient, $\vec{n}$ the unit vector from the nearest point on the reference wall, G_1 and G_1 functions of the nondimensional wall distance s. s is the distance from the particle to the reference wall normalized by D_h.

$\vec{F}_{External}$ on Equation. 3.14 refers to the additional forces acting on the particle when the device is subjected to electrical, magnetic, or acoustic fields.

3.3 Acoustophoresis

Acoustophoresis is the manipulation of particles using acoustic waves. It is a non-contact and label-free method, so it is being applied to biomedical applications for particle and cell separation [32-36].

The acoustic waves are generated by applying alternating voltage in transducers made of piezoelectric materials [16]. Piezoelectric materials generate mechanical motion when an electric field is applied. The type of vibration is usually categorized in two major groups: Bulk acoustic waves (BAWs) and Surface Acoustic waves (SAWs).

Surface acoustic waves (SAWs) is the type of vibration which happens only on the surface of an elastic material [16]. SAW-based devices have the advantage over BAW-devices of not having geometry or material restrictions, they can be of soft-polymer materials commonly used in microfluidic applications, such as PDMS, and are easy to miniaturize [29]. SAW propagates along the solid-fluid interface and decreases exponentially with the solid body depth [48]. They are generated by applying a signal to interdigitated transducers (IDTs) deposited on top of a piezoelectric crystal (Figure 11).

An IDT consists of two sets of spatially periodic electrodes, overlapped and opposite faced, with several fingers in parallel between them.

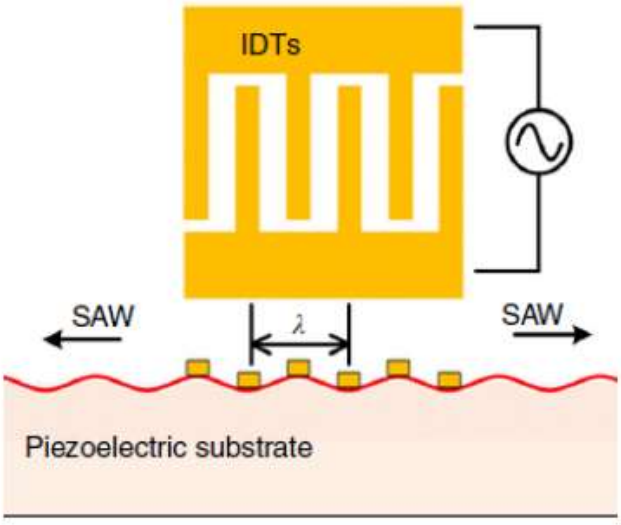

Figure 11 Schematic representation of an IDT on a piezoelectric substrate [48]

The wave propagates perpendicular to the electrode-fingers in the IDT. The frequency f of the acoustic wave is defined by $f = v/\lambda$, where v is the sound speed in the piezoelectric material and λ is the acoustic wavelength [48]. The wavelength of SAW is dependent on the width and spacing between IDT fingers (Figure 11). When the width and spacing of IDTs fingers are equal, the generated SAW will have a wavelength of 4 times the width of the IDTs. SAW devices can work at very high frequencies [49], having as limitation the size of the channel, since particles would start to collect at the walls. A SAW field can be generated by placing the microchannel between 2 pairs of IDTs and making SAWs travel in opposite directions. The interference results in a standing surface acoustic wave (SSAW) field between the two IDTs (Figure 12). Standing acoustic waves form minimum and maximum pressure regions in the fluid called pressure nodes and antinodes. Cell separation forces are generated in this periodic fluctuation of pressure, since particles experiencing larger acoustic forces will be attracted to the pressure nodes.

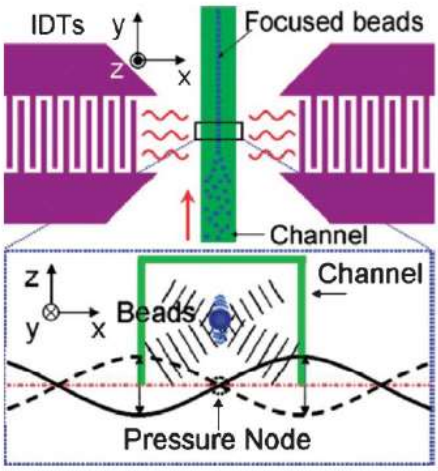

Figure 12 Schematic representation of a SSAW device and its working mechanism[52]

Bulk acoustic waves (BAWs) are generated when the whole body of piezoelectric material vibrates [46]. Channels of the devices based on this kind of waves are made of materials with excellent acoustic reflection properties [47], such as silicon and glass; to be able to reflect the waves. BAW-based devices have the advantage of a simple architecture since they don't have IDTs. The channel is placed on top of a piezoelectric material. When AC signal is applied, the piezoelectric materials vibrate at the frequency of the AC signal. The acoustic pressure field is formed by making the width of the channel match half-integer multiples of the wavelength of the frequency applied [46]. Figure 13 shows the schematic of a cross section of a BAW-based device. Nodes and antinodes are formed in the fluid domain and particles will be attracted to them.

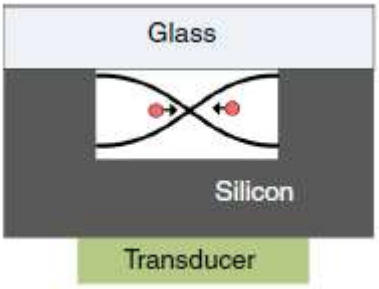

Figure 13 Schematic representation of a BAW device and its working mechanism[16]

Particles exposed to an acoustic wave field will be affected by an acoustic radiation force. The force will cause the motion of the particle depending on the particle properties with respect to the surrounding medium.

Bruus [50] presented the theoretical derivation of the expression for the acoustic radiation force on a compressible spherical particle suspended in a fluid with acoustic waves, which was first generalized by Gorkov. It is based on the ultrasound's perturbations of density, pressure, and velocity. By using the scattering theory, the equation for calculating the acoustic radiation force $\vec{F}_{rad}$ on a small, spherical particle is the gradient of an acoustic potential U_{rad} [40, 50]:

$$\vec{F}_{rad} = -\nabla U_{rad} \tag{3.18}$$

$$U_{rad} = \frac{4\pi}{3} {r_p}^3 [f_1 \frac{1}{2} k_f \overline{\mathrm{p}^2} - f_2 \frac{3}{4} \rho_f \overline{\mathrm{V}_{\mathrm{in}}^2}] \tag{3.19}$$

$$f_1 = 1 - \frac{k_p}{k_f} \tag{3.20}$$

$$f_2 = \frac{2(\rho_P - \rho_f)}{2\rho_P + \rho_f} \tag{3.21}$$

$$k_f = \frac{1}{\rho_f c_f^2} \tag{3.22}$$

Where U_{rad} is the acoustic potential energy, f_1 and f_2 are the scattering coefficients, p the external pressure of the acoustic field, V_{in} the incoming velocity, k_p the compressibility of the particle, k_f the compressibility of the fluid, and c_f the speed of sound in the fluid. The line over the expressions are time averages over an oscillation period. This is only valid for small particles comparing to the wavelength $r_p/\lambda \ll 1$ [51].

Chapter 4

Methods

This chapter presents the model developed for simulating the acoustophoretic centrifugal microfluidic platform. The model is first used to simulate SAWs. The attempt to validate it with an experimental work is described, and then its validation with a simulation work is included. A parametric analysis to study the influence of different parameters on the efficiency of the platform is presented. Then, a BAWs-based platform approach is taken to try to match results with experimental works, the attempt to validate it is described.

4.1 Simulation method SAWs-based platform

A three-dimensional Finite Element Method (FEM) analysis was built in COMSOL to simulate separation of cells using SAWs in a centrifugal microfluidic platform. COMSOL is a FEM-based simulation software appropriate for analysis of multiple physics. The Multiphysics included in the model were the piezoelectric effect and the acoustic-structure interaction. The first one involves the physics of electrostatics and solid mechanics, and the second one the pressure acoustics. Additionally, the physics of creeping flow of single-phase, and particle tracing for fluid flow were added.

The 3D model geometry consists of 2 pairs of IDTs located on top of a piezoelectric substrate, with a fluid channel between the IDTs. The model starts with the linear piezoelectric constitutive equations which govern the propagation of SAW in the piezoelectric substrate [53, 54]:

$$S = S_E T + e^t E \tag{4.1}$$

$$D = eS + \varepsilon_0 \varepsilon_r E \tag{4.2}$$

Where T is the stress, S the strain, D the charge density displacement, and E the electric field. S_E is the compliance matrix, ε_0 the permittivity of free space, ε_r the permittivity matrix, and e the piezoelectric coupling matrix. By applying the boundary conditions, material properties and the input parameters, explained in the next sections, to the geometry, stress and strain are obtained within the solid materials.

The pressure of the channel flow is assumed to be the same as the normal stress of the substrate in contact to the channel [54]:

$$\sigma \mathrm{n} = -\mathrm{p} \cdot \mathrm{n} \tag{4.3}$$

By knowing this, the Helmholtz equation can be solved to determine the acoustic pressure field and the incoming velocity in the fluid:

$$\nabla^2 p = \frac{\omega^2}{c_f^2} p \tag{4.4}$$

$$\vec{V_i} = \frac{-\nabla p}{\omega \rho_f} \tag{4.5}$$

where $c_f$is the speed of sound in the fluid, $\rho_f$the density of the fluid, ω the angular frequency, p the acoustic pressure, and $\vec{V_i}$ the incoming velocity. The acoustic pressure and incoming velocity are used for solving the acoustic radiation force in the last step.
Next, the fluid mechanics equations are solved to obtain the velocity field in the channel. By assuming incompressible fluid and neglecting gravity, Equation 3.2 becomes:

$$\rho_f \frac{\partial \vec{V}_f}{\partial t} = -\nabla p + \mu_f \nabla^2 \vec{V}_f + \vec{f}_b \tag{4.6}$$

Because a rotational platform is considered, the centrifugal forces become the body forces:

$$\rho_f \frac{\partial \vec{V}_f}{\partial t} = -\nabla p + \mu_f \nabla^2 \vec{V}_f + \vec{f}_{centrifugal} + \vec{f}_{Coriolis} \tag{4.7}$$

$$\rho_f \frac{\partial \vec{V}_f}{\partial t} = -\nabla p + \mu_f \nabla^2 \vec{V}_f - \rho_f \vec{\omega} \times (\vec{\omega} \times \vec{r}) - 2\rho_f \vec{\omega} \times \overrightarrow{V_f} - \rho_f \frac{d\vec{\omega}}{dt} \times \vec{r}$$

The assumption of constant velocity is considered, so Euler force is neglected.
Finally, to obtain the exact path of particles, the particle equations of motion are solved. By considering the centrifugal forces, the drag and lift (wall-induced) forces, and the acoustic radiation force as the external force, Equation 3.14 becomes:

$$m_p \frac{d\vec{V}_p}{dt} = \vec{F}_{centrifugal} + \vec{F}_{Coriolis} + \vec{F}_{Drag} + \vec{F}_{Lift} + \vec{F}_{Rad} \tag{4.8}$$

The Acoustic radiation force considered in the model was the one the software COMSOL has as default, which is equivalent to equations 3.18-3.22:

$$\vec{F}_{rad} = -2\pi {r_p}^3 [\frac{1}{3} K_{s_1} Re(f_2 \mathrm{p} * \nabla \mathrm{p}) - \frac{1}{2}\rho_f Re(f_2 V_{in} * \nabla V_{in})] \quad (4.9)$$

$$f_1 = 1 - \frac{k_{s,p}}{k_s} \quad (4.10)$$

$$f_2 = \frac{2(\tilde{\rho}-1)}{2\tilde{\rho}+1} \quad (4.11)$$

$$\tilde{\rho} = \frac{\rho_p}{\rho} \quad (4.12)$$

$$k_f = \frac{1}{\rho_f c_f^2} \quad (4.13)$$

$$k_p = \frac{1}{\rho_p (c_{p,p}^2 - \frac{4}{3} c_{s,p}^2)} \quad (4.14)$$

Considering solid particles, the default values of pressure-wave speed $c_{p,p}$ and shear wave speed $c_{s,p}$ were 2400 m/s and 1150 m/s respectively.

4.2 Boundary conditions SAWs-based platform

The boundary conditions applied in the model are of zero normal displacement at two parallel sides of the substrate and stress free at the other boundaries. The substrate is a piezoelectric material, and electric potential gradients on it cause an elastic wave propagation [53]. Initial values are assumed to be zero. A sinusoidal voltage is applied to the IDTs by adding a voltage value to half of IDTs, and by keeping the other half as ground V=0. Charge conservation piezoelectric material was used for the substrate. The channel is subjected to acoustic pressure. Normal stress of the substrate in contact with the channel is assumed to be the same as the pressure of the channel flow. The inertial effects are considered negligible because they are small compared to viscous effects, so creeping flow is assumed in the channel. Non-slip boundary condition is applied to the walls of the channel. Inlets and outlets are considered to be at atmospheric pressure.

4.3 Model validation SAWs-based platform

4.3.1 Model validation experimental work SAWs-based platform

The 3D model was tried to be validated with the experimental work performed by Shi et al. [29]. The geometry consisted of a channel of 150 μm in width, 80 μm in height, and the length of 900 μm was used to reduce the computational time, and because the authors expressed the separation was done in the first 600 μm of the channel. Three inlets and three outlets of 50 μm each one are considered in the channel. Two pairs of IDTs with a pitch of 150 μm and finger's width of 75 μm are placed on top of a Lithium Niobate substrate in order to generate a wavelength of 300 μm and therefore, apply a frequency of 13 MHz. Polystyrene particles of 4.17 μm and 0.87 μm in diameter, and 1.04 g/cm^3 in density were used in the experimental work. Experimental work used a non-centrifugal microfluidic platform, therefore, for the simulation the centrifugal forces at the creeping flow and at the particle tracing are disabled. The boundary condition of the inlets changes to normal velocity of 1 mm/s at the sided inlets, where sample enters, and to 5.2 m/s to the center inlet, where the sheath flow enters. With these input data, the acoustic pressure field in the channel was simulated.

4.3.2 Model validation simulation work SAWs-based platform

The model was then validated by using as input data the simulation work performed by Shamloo et al. [54]. The geometry consisted of a channel of 100 μm in width, 50 μm in height, and 600 μm in length. Two sided inlets with a tilted angle of 30º are added at the left of the channel for the sample entrance, leaving the center inlet for the sheath flow entrance. Three outlets are added to the right of the channel, with the two at the sides with tilted angle of 45º. 2 pairs of IDTs with 5 fingers at each side are used. The dimensions of the fingers are 200 μm in length, 10 μm in width, and a separation of 10 μm between each finger. In this work, platelets are separated from WBCs and RBCs by using particles with diameters of 2-4 μm to simulate platelets, 6-8 μm for RBCs and 12-15 μm for WBCs. All of them with density of 1020 kg/m^3. A non-centrifugal microfluidic platform is used in Shamloo's work, therefore, the centrifugal forces in the model are disabled and the boundary condition of the inlets changes to normal velocity of 15 mm/s

at the side-inlets and 30 m/s at the center-inlet. The frequency applied in this work was of 7.4125 MHz. This value was obtained using the equation first presented by Bruus [57], which is used for generating a pressure node in the middle of a rectangular channel:

$$\mathrm{f} = \frac{c_f}{2w} \tag{4.9}$$

were w is the width of the channel and c_f the speed of sound of water.

80V was the voltage applied to replicate the results from Shamloo. With these input data, the acoustic pressure field in the channel and the particle path of the particles are generated and compared with the work presented by Shamloo.

4.4 Geometrical configuration SAWs-based platform

A fixed geometry for the acoustophoretic separation device is proposed to continue with the parametric analysis. It is based on Shamloo's work [54] with inlet and outlets modifications to improve the acoustic pressure field. The acoustophoretic platform consists of three parts, as shown in Figure 14; the piezoelectric substrate, the channel, and 2 pair of IDTs. The substrate is a rectangle of 1500 μm in length, 750 μm in width and 100 μm in height. IDTs are placed on top of the substrate, parallel one to each other, and the channel is situated between them. IDTs consist of 5 fingers, each one with 200 μm in length, 10 μm in width and 10 μm in height. Separation between each overlapped finger is of 10 μm, so a pitch of 20 μm is obtained. The distance of each pair of IDTs to the channel is of 70 μm. The channel consists of a main rectangular channel of 600 μm in length, 100 μm in width, and 50 μm in height, placed at the middle of the substrate. Three inlets are situated at the left side of the channel. Each inlet is 40 μm in length and 33.33 μm in width. The center-inlet is used as the entrance of sheath flow. The two inlets at the side are tilted with an angle of 30º and are used as the entrance of the sample flow. Three outlets are situated at the right side of the channel with the same dimensions of the inlets. The sided outlets collect the particles with lower diameter and the center outlet collects the largest particles.

The mesh used for the simulation (Figure 15) consisted of a triangular mesh with 7.71 μm as maximum element size for the IDTs, 12.4 μm for the channel and 82.5 μm for the substrate. Corner refinement is added to the corners of the channel.

To make a centrifugal device, the SAW separation platform needs to be placed on a disc, as Figure 16 shows. For the simulation, the centrifugal forces were added with a distance *r* from the axis of rotation, with an angular velocity ω in the counterclockwise direction. The geometry proposed is with the channel aligned radially to the center of rotation.

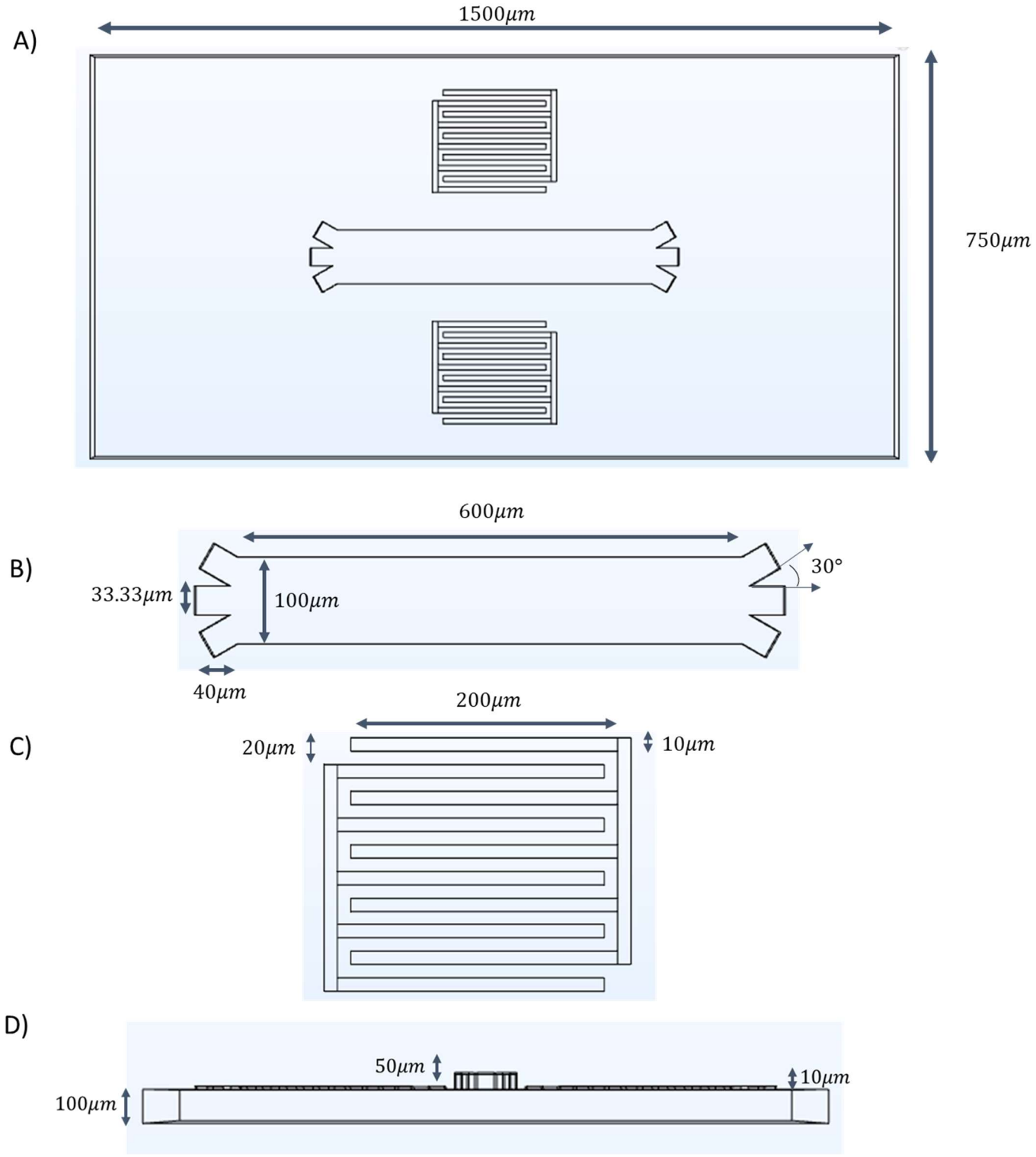

Figure 14 Geometry of the SAW platform. A) Top view. B) Zoom of the channel. C) Zoom of the IDT. D) Lateral view

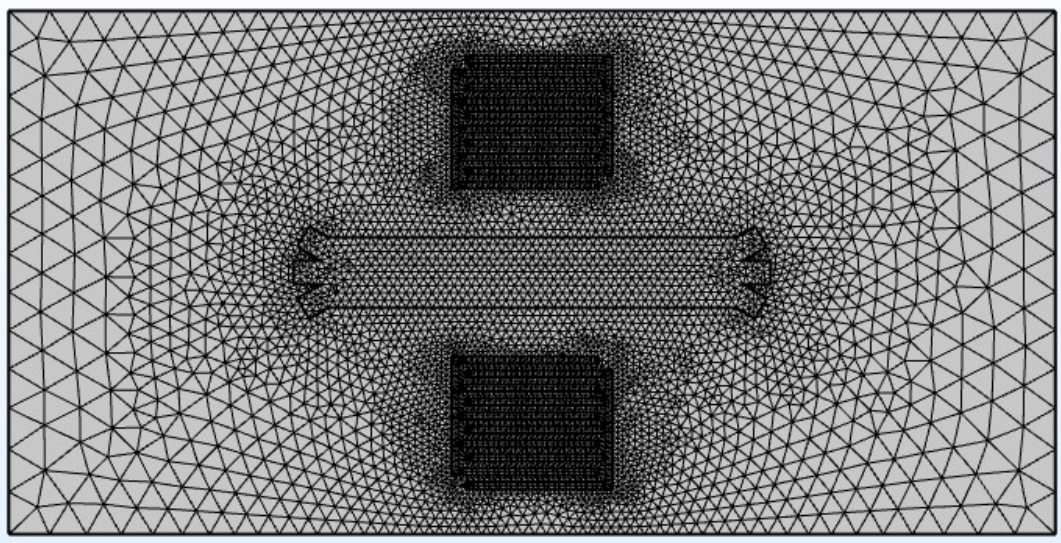

Figure 15 Mesh used for the simulation

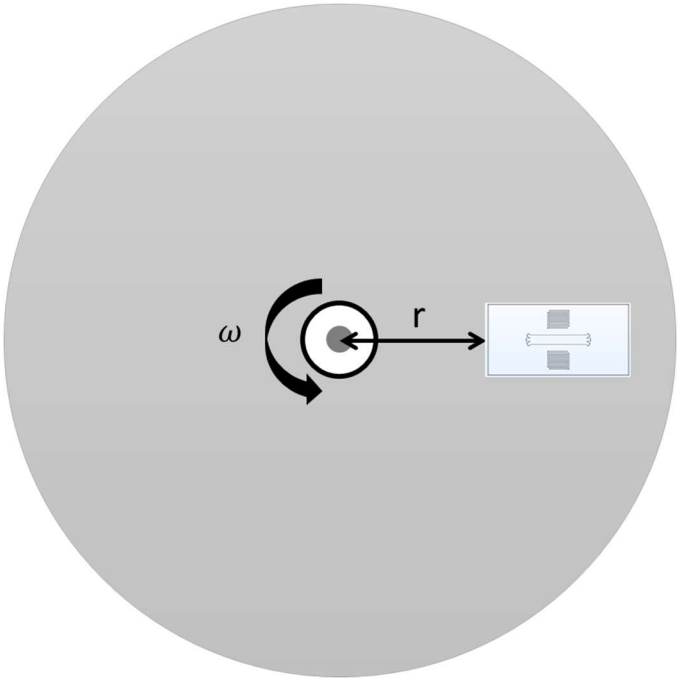

Figure 16 SAW platform placed on a disc

4.5 Material properties and input parameters SAWs-based platform

The piezoelectric substrate is established as Lithium Niobate $LiNbO_3$ since it is the material preferred in acoustic wave devices according to previous works [32-36]. IDTs are assumed to be deposited layers of Aluminum (Al), and the channel is assumed to be filled with water. Table 2 shows the properties of the materials used, which were values from COMSOL's materials library.

Table 2 Input parameters: Properties of the materials used in the simulation [54, 58]

	Modulus of elasticity (C_E)	**Density (ρ)**	**Relative permittivity (ε_r)**	**Coupling Matrix (e_E)**
$LiNbO_3$	242.4 GPa	4700 kg/m^3	{43.6, 43.6, 29.16}	{0, -2.53764, 0.193644, 0, 2.53764, 0.193644, 0, 0, 1.30863, 0, 3.69548, 0, 3.69594, 0, 0, -2.53384, 0, 0} C/m^2
Al	70GPa	2700 kg/m^3	1	

The model proposed is intended to separate CTCs from blood samples, so particles with similar characteristics to CTCs, WBCs, and RBCs are used. For model simplification, rigid sphere particles are assumed, with diameters of 20 μm, 10 μm and 8 μm for CTCs, WBCs and RBCs respectively [19, 34, 20]. The density was established as 1070 kg/m^3, 1080 kg/m^3, and 1110 kg/m^3 for CTCs, WBCs and RBCs respectively [56, 18]. Even though in real life cells are not spherical, the acoustic force theory makes this assumption. The acoustic force does depend on the compressibility of the particles, however, experimental works [36] have tested their devices first with rigid particles and then with real cells, cells being not rigid, and separation efficiency difference was only of 4%, so the assumption of rigid particles was taken for model simplification.

The input parameters used for the simulation of the geometry proposed were the voltage applied to the IDTs to generate the electric field, and the angular velocity and distance to

the axis of rotation to simulate the rotation of the platform. These values are listed on Table 3. However, they were later modified in order to study their influence on the efficiency of the device. The initial fixed values are presented on Table 3.

Table 3 Input parameters: Voltage, rotation parameters, frequency, and particle properties.

Parameter	Value
Voltage	15 V
Angular Velocity	50 rad/s
Distance to the axis of rotation (radius)	2.5 cm
Frequency	7.4125 MHz
Particle diameter	20 μm CTCs 10 μm WBCs 8 μm RBCs
Particle density	1070 kg/m^3 CTCs 1080 kg/m^3 WBCs 1110 kg/m^3 RBCs

4.6 Parametric study SAWs-based platform

For evaluating the separation efficiency, the recovery rate is the parameter frequently used [43]. It is defined as the ratio of the number of targeted particles collected in the specific outlet to the total number of those particles in the inlet. Another important parameter to study is the purity of the separation. Purity refers the percentage of the number of targeted particles over the total number of collected particles in the specific outlet [33]. These values for CTCs, WBCs and RBCs are obtained for different configurations of the proposed device in order to find the optimal performance.

The recovery rate and purity were calculated by filtering the final position on the y-axis of all the particles. Because of the geometry used, a final position between -16.667 and 16.667 μm corresponds to the center outlet. Values out of these range correspond to the

sided outlets. Position of particles at the x-axis was also examined since it needed to be at least 1050 μm for being considered in the outlets.

Input parameters of the proposed device for the model simulation are shown in Table 3. The influence of some of these parameters on the separation performance of CTCs with blood components is analyzed. Table 4 shows the range of values of the angular velocity, voltage, and distance to axis of rotation (radius) used for the analysis; while the frequency, and the particle properties were kept fixed. To reduce the computational time and for an easier study, the simulation was performed with an equal proportion of 50 CTCs, 50 WBCs and 50 RBCs.

Table 4 Values of first parametric study

Angular velocity (rad/s)	**Voltage (V)**	**Radius (cm)**
Study 1		
40	15	2.5
50	15	2.5
60	15	2.5
70	15	2.5
Study 2		
50	13	2.5
50	15	2.5
50	17	2.5
50	19	2.5
Study 3		
50	15	1.5
50	15	2
50	15	2.5
50	15	3

Additionally, a parametric study with the geometry of the device was performed. It included the distance of IDTs with respect to the channel and the tilted angle of the channel with respect the rotational axis. This last parameter is described in Figure 17 and is the result of giving values to r_1 and r_2. It was assumed to be zero previously because the channel was aligned radially, so r_2 was zero. Table 5 presents the range of values used for these studies.

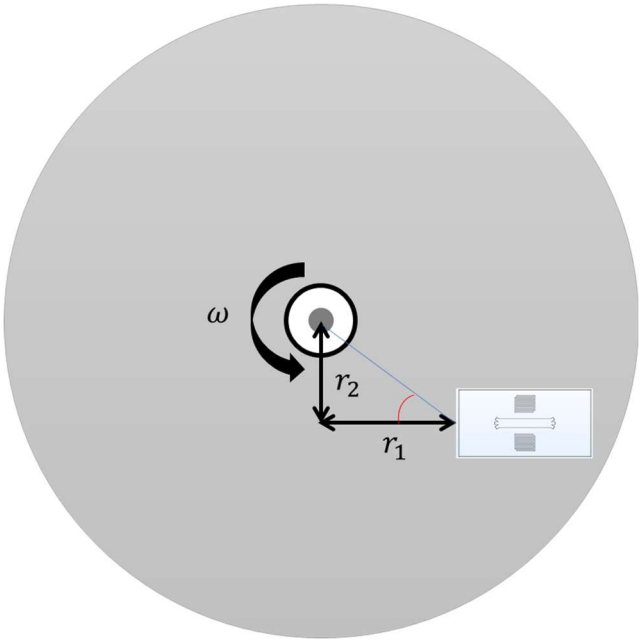

Figure 17 SAW platform placed on a disc with tilted angle.

Table 5 Values of second parametric study

IDTs-channel distance (um)	Tilted angle
Study 4	
50	0
70	0
90	0
110	0
Study 5	
70	15º
70	30º
70	45º
70	60º

The tilted angle of Study 5 was obtained by setting r_1 as 2.5 cm and by giving the following values to r_2:

Table 6 Values of r2

Tilted angle	r_2
15	0.67
30	1.44
45	2.5
60	4.33

Because the concentration of CTCs on blood samples is usually extremely low, a study with different proportions of CTCs and blood components was also performed. The separation efficiency and purity were calculated using 10 CTCs, and 1000 WBCs and RBCs, with input parameter values listed on Table 3.

4.7 Comparison with non-centrifugal device SAWs-based platform

The recovery rate and purity of the centrifugal device proposed for particle and cell separation through acoustophoresis was compared to a non-centrifugal device, with the same input parameters (Table 3). In order to simulate the non-centrifugal device the centrifugal forces at the creeping flow and at the particle tracing were disabled, and the boundary condition at the inlets changed to normal inflow velocity instead of atmospheric pressure. The inflow velocities established were 8.3 mm/s for the center inlet, 7.83 mm/s for the upper side inlet, and 7.9 mm/s for the lower side inlet. With these values, the average velocity magnitude at the channel on both devices, centrifugal and non-centrifugal, was of 7.4 mm/s.

Additionally, the sensibility of the device with particle density variation and fixed diameter was analyzed and compared between the centrifugal and non-centrifugal platform, configuration which can be useful in other applications. The range of particles density was 1050-1170 kg/m^3, and the diameter considered 15 μm.

4.8 Simulation method BAWs-based platform

Another approach was taken in order to try to match simulation results with experimental works, and a BAWs-based platform was simulated. To accomplish it, the method and boundary conditions described in section 4.1 and 4.2 are used. The difference relied on the removal of IDTs, and therefore, the voltage is instead applied to the bottom layer of the piezoelectric substrate, while the top layer is set as ground V=0.

4.9 Model validation BAWs-based platform

The model was tried to be validated by using as input data the experimental work performed by Dykes et al. [26] which separates platelets from WBCs in an acoustophoretic-based platform. The geometry consisted of a channel of 380 μm in width

with three inlets and three outlets. The length and height of the channel were not stated, so they were assumed to be 6 mm and 50 μm respectively. The channel was placed centered on top of a piezoelectric material with 5 mm in length, 760 μm in width, and 50μm in height. For simulating platelets, spherical solid particles are used with 2 and 4 μm in diameter and 1058 kg/m^3 in density; while WBCs are assumed to be 10 and 12 μm in diameter and 1080 kg/m^3 in density. The simulation was performed with a total of 50 particles of each size in order to evaluate the separation efficiency. The centrifugal forces were disabled because the experimental work used a non-centrifugal microfluidic platform. The boundary condition at the inlets is changed to normal velocity of 33 mm/s at the sided inlets, where sample enters, and to 75 mm/s to the center inlet, where the sheath flow enters. These velocities were calculated using the transverse areas of the inlets and the flow rates mentioned on the paper, 40 μL/min on the center-inlet and 10 μL/min on the side-inlets. The piezoelectric material used in the experimental work is PZ-26, and Table 7 shows its properties needed for the simulation.

Table 7 Input parameters: Properties of PZ-26 [59]

	PZ26
Density (ρ)	7700 kg/m^3
Elasticity matrix (C_E)	{168, 110, 168, 99.9, 99.9, 123, 0, 0, 0, 30.1, 0, 0, 0, 0, 30.1, 0, 0, 0, 0, 0, 28.8} [GPa]
Coupling Matrix (e_E)	{0, 0, -2.8, 0, 0, 2.8, 0, 0, 14.7, 0, 9.86, 0, 9.86, 0, 0, 0, 0, 0} [C/m^2]
Relative permittivity (ε_r)	{828, 828, 700}

The frequency applied is 2MHz since the width of the channel is 380 μm. The acoustic pressure field was generated and the path of the cells was simulated.

Chapter 5

Results

This chapter presents the outcomes of the model validations and the results obtained after the implementation of the model on different configurations of the device.

5.1 Model validation SAWs-based platform

5.1.1 Model validation experimental work SAWs-based platform

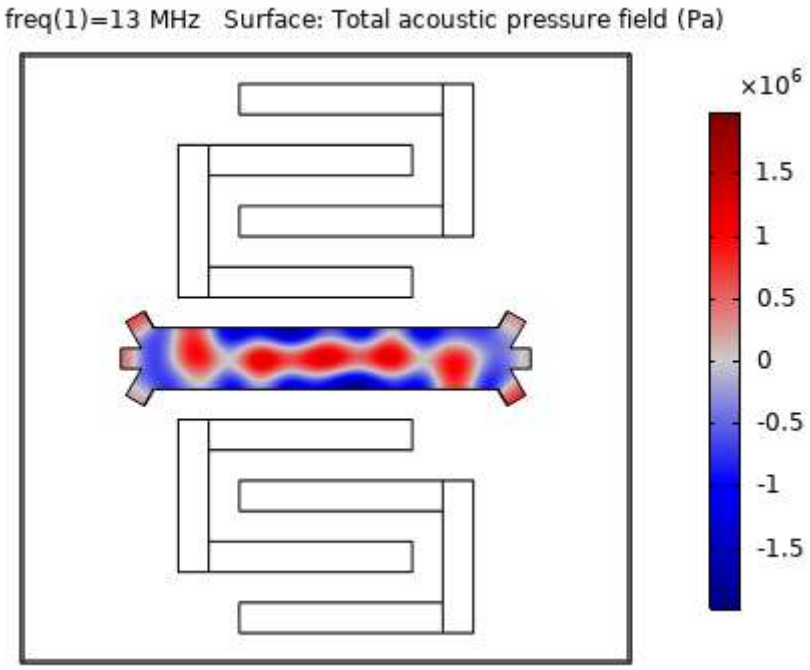

Figure 18 Acoustic pressure field of the model validation based on Shi et al work

An attempt to simulate the experimental work performed by Shi et al. (2009) for particle separation in an acoustophoretic microfluidic device was done. However, it was not achieved since the acoustic pressure field was not generated correctly. Pressure minimum and maximum regions are essential since particles will move through them. For larger particles to be collected in the center inlet, and smaller particles at the side inlets, as Shi et al did in their experiment, a region of minimum pressure or pressure node needs

to be generated in the center of the channel. However, this did not happen as Figure 18 shows. The geometry of the device and the frequency applied are the inputs that change the acoustic pressure field. However, even by changing the dimensions not specified in the paper, the acoustic field did not show the pressure node in the center of the channel.

5.1.1 Model validation simulation work SAWs-based platform

The model was then validated by using the geometry and input parameters of the work performed by Shamloo. The acoustic pressure field is obtained and shown in Figure 19. It can be seen how the pressure node is generated correctly at the center of the channel, which makes possible the particle separation in the next step.

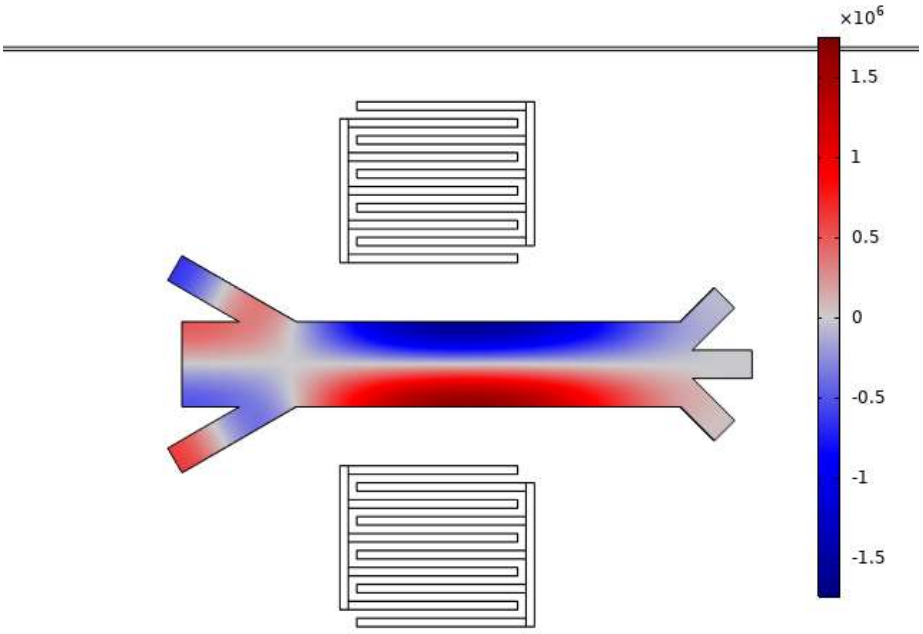

Figure 19 Acoustic pressure field of the model validation based on Shamloo's work

Figure 20 shows the particle path of platelets in dark blue, RBCs in light blue, and WBCs in red. A and B are figures of Shamloo's paper, and C and D are figures of the simulation developed. These figures show that the paths generated in the simulation matches Shamloo's work. The sample enters by the sided inlets, and larger particles (WBCs and RBCs) are moved to the centerline of the channel due to the pressure node generated. Smaller particles (platelets) stayed next to the walls and collected by the sided outlets.

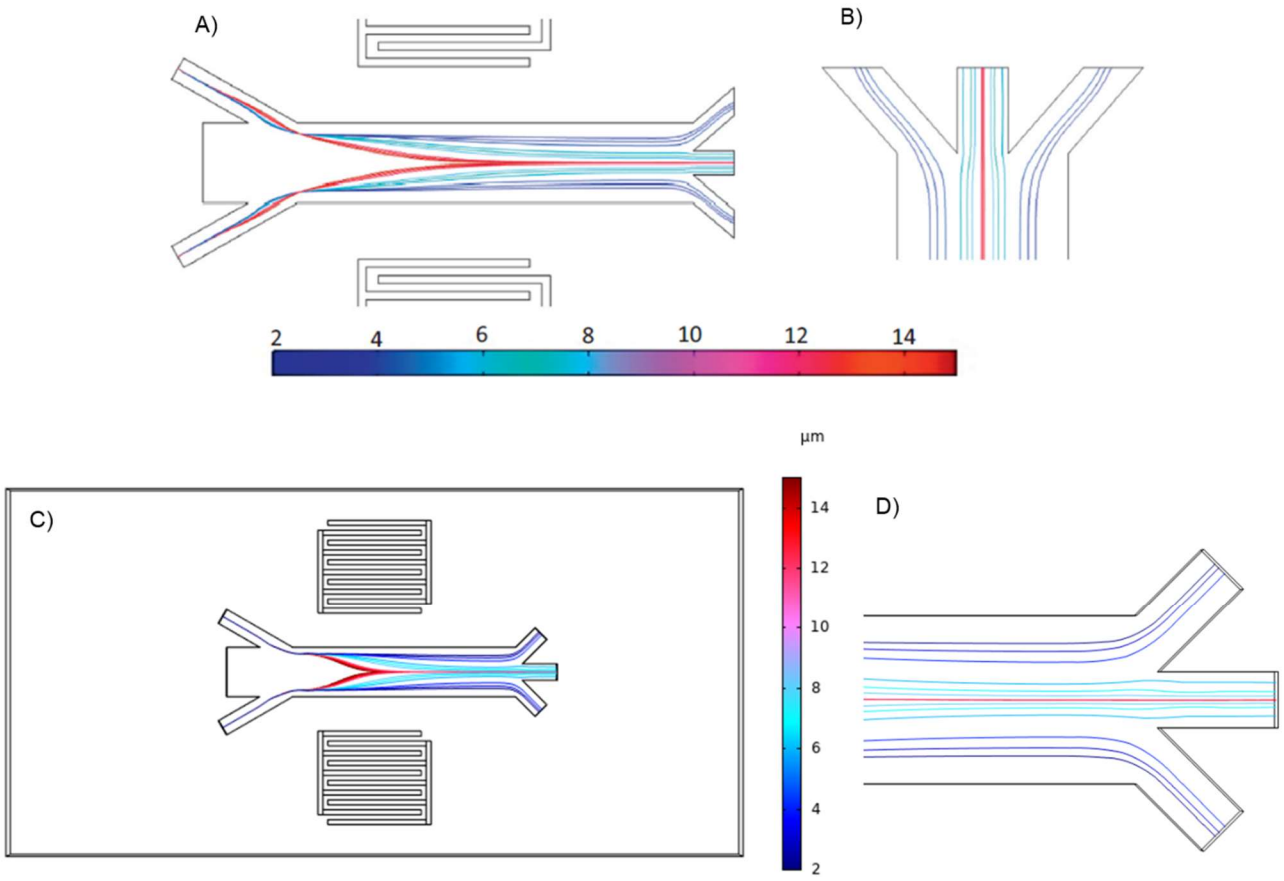

Figure 20 Particle path of platelets in dark blue, RBCs in light blue, and WBCs in red. A) Shamloo's results [54] B) Zoom of the outlets of Shamloo's results C) Simulation's results D) Zoom of the outlets of the simulation

5.2 Parametric study SAWs-based platform

Results of the parametric study on the SAWs-based platform are presented on the following subsections.

5.2.1 Angular velocity

Figure 21 presents the recovery rate and purity of CTCs, WBCs and RBCs at different dimensionless angular velocities. The applied angular velocity is transformed to a dimensionless value by dividing it with a reference angular velocity ω_0 . The reference value was set to the first one applied, 40 rad/s for this case. Figure 21A shows how the recovery rate of CTCs at the center-outlet decreases as the velocity increases. This happens because particles stayed less time in the acoustic field, and they are not completely focused to the pressure nodes. The recovery rate of CTCs was the highest and remained almost constant for a dimensionless angular velocity of 1, meaning, the largest number of CTCs were collected at the center-outlet with this velocity. The highest recovery rate of WBCs and RBCs at the side outlets was obtained at 1.75.

Purity was also calculated at the center and side outlets. The highest purity value of blood cells at the side outlet was obtained at 1-1.25, meaning, at this angular velocity, no CTCs ended on the side-outlets. Purity of blood cells at the side outlet decreases as the angular velocity increases for the same reason explained before, CTCs are not completely moved to the pressure nodes because they pass too fast through the acoustic field. The highest purity of CTCs at the center outlet was at 1.25-1.5

If the main objective of the separation is to collect most of CTCs at the center-outlet, making the effort to not lose them on the side-outlets, the values to put more attention would be the highest CTCs recovery rate, and the highest purity of blood cells at the side outlets. After this priority, it would also be liked to maintain high the recovery rate of WBCs and RBCs, and the purity of the center outlet. Knowing this, the non-dimensional angular velocity recommended would be 1.25. which in this case it would be 50 rad/s.

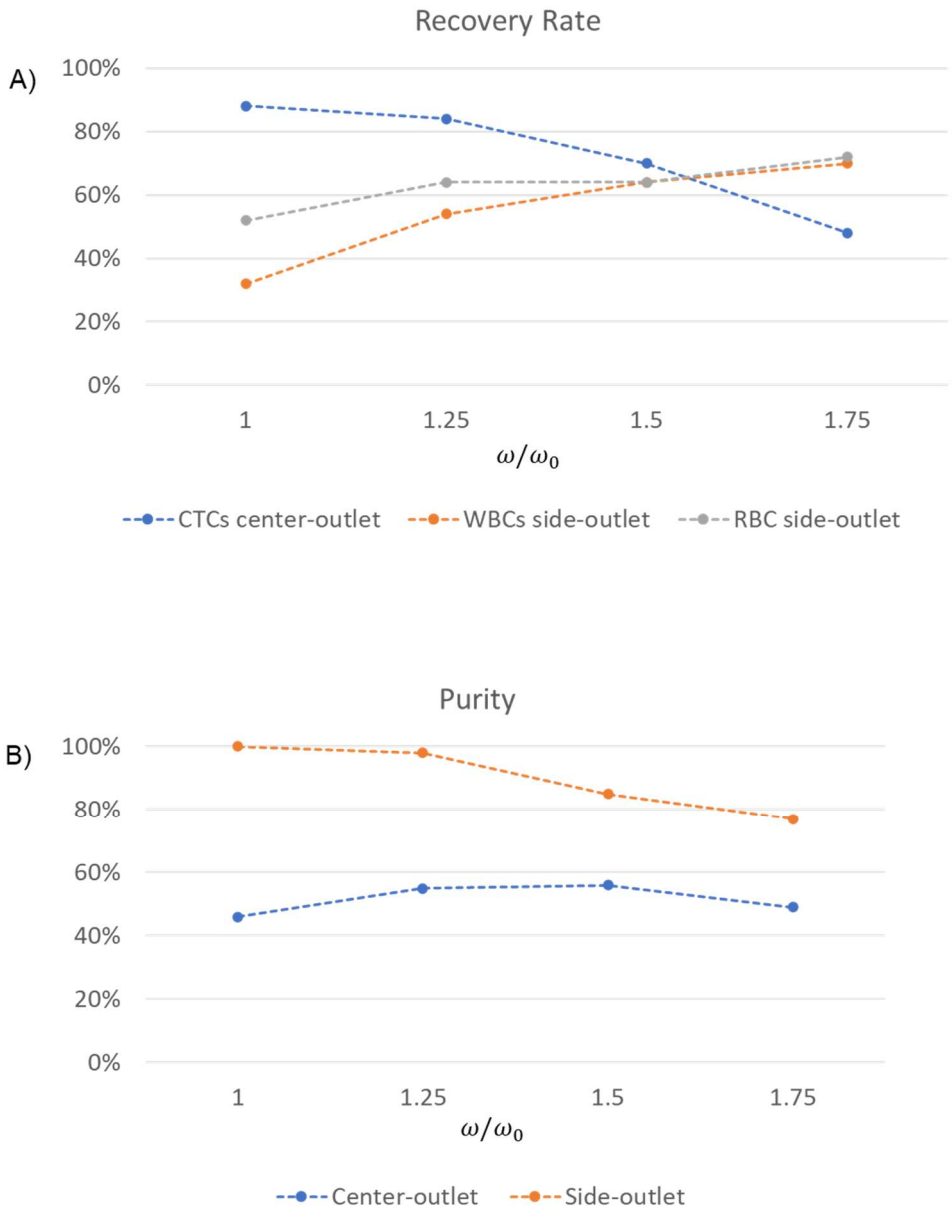

Figure 21 Recovery rate for CTCs, WBCs and RBCs at different angular velocities B) Purity at the outlets at different angular velocities

5.2.2 Voltage

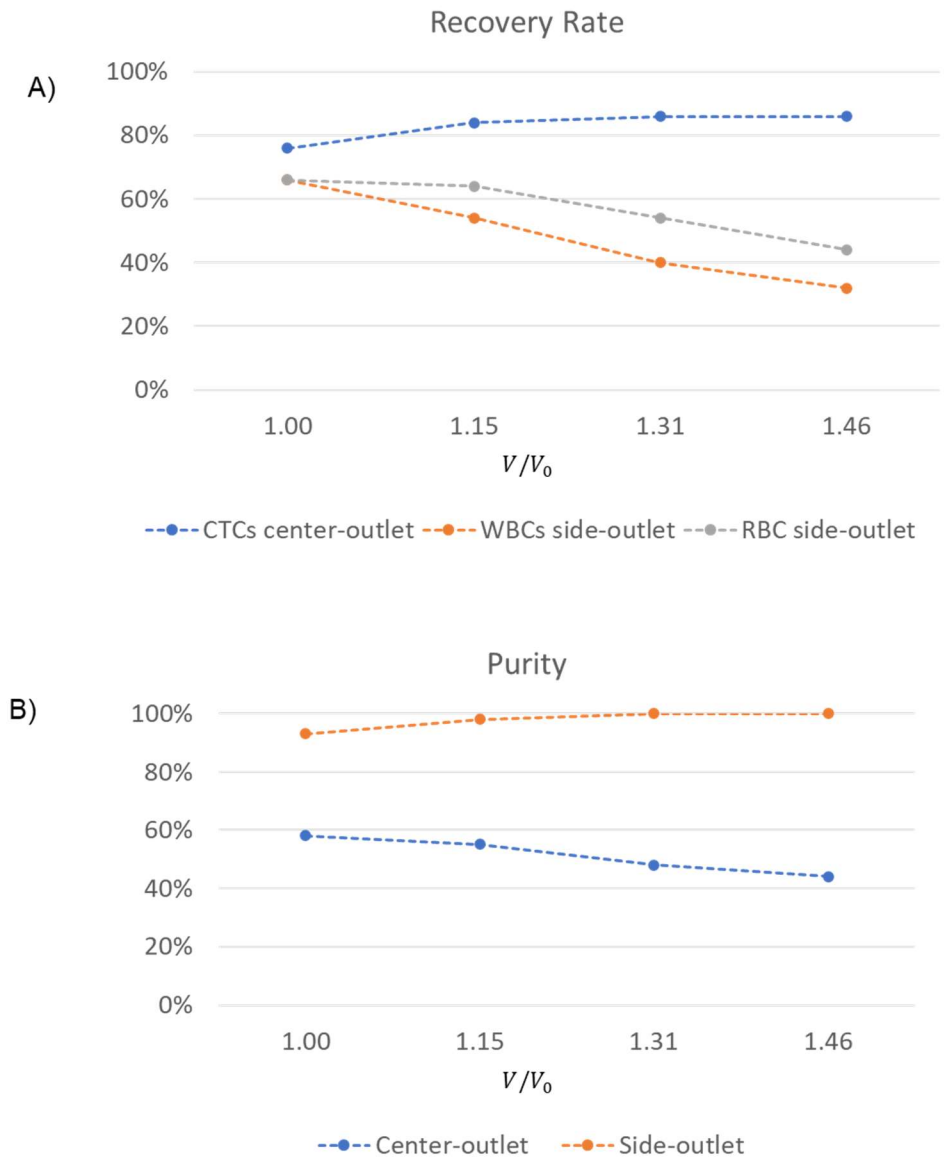

Figure 22 Recovery rate for CTCs, WBCs and RBCs at different voltages B) Purity at the outlets at different voltages

Figure 22 presents the recovery rate and purity of CTCs, WBCs and RBCs at different dimensionless voltage. The applied voltage is transformed to a dimensionless value by dividing it with a reference value V_0. The reference voltage was set to the first one applied, 13 Volts for this case. Figure 22 shows that the CTCs recovery rate and the blood cells

purity at the side-outlets tend to increase as the voltage increases. This happens because the acoustic pressure generated on the channel increases, so CTCs moved easier to the pressure nodes and further to the center-outlet. However, both parameters almost stabilize after reaching certain value. The highest recovery rate value for CTCs was obtained at 1.15-1.46, and the highest purity value of blood cells at the side-outlet was obtained at the same voltage values. From these voltage values, the recommended one is 1.15 since the purity of CTCs at the center outlet is higher. It corresponds to 15V in this example.

5.2.3 Distance to axis of rotation

Figure 23 presents the recovery rate of CTCs, WBCs and RBCs at different dimensionless radius. The radius *r* refers to the distance of the SAW platform to the axis of rotation, which is the center of the disc. The radius *r* is transformed to a dimensionless value by dividing it with the radius of the disc *R*. The radius of the disc used is 6cm. The CTCs recovery rate and the blood cells purity at the side-outlets decrease if the radius increases more than 0.4. This could have happened because the angular velocity increases at higher distance from the axis of rotation, so CTCs pass too fast through the acoustic field and are not completely moved to the pressure nodes. The recommended dimensionless radius would be 0.4, which in this case corresponds to the distance of 2.5cm from the axis of rotation.

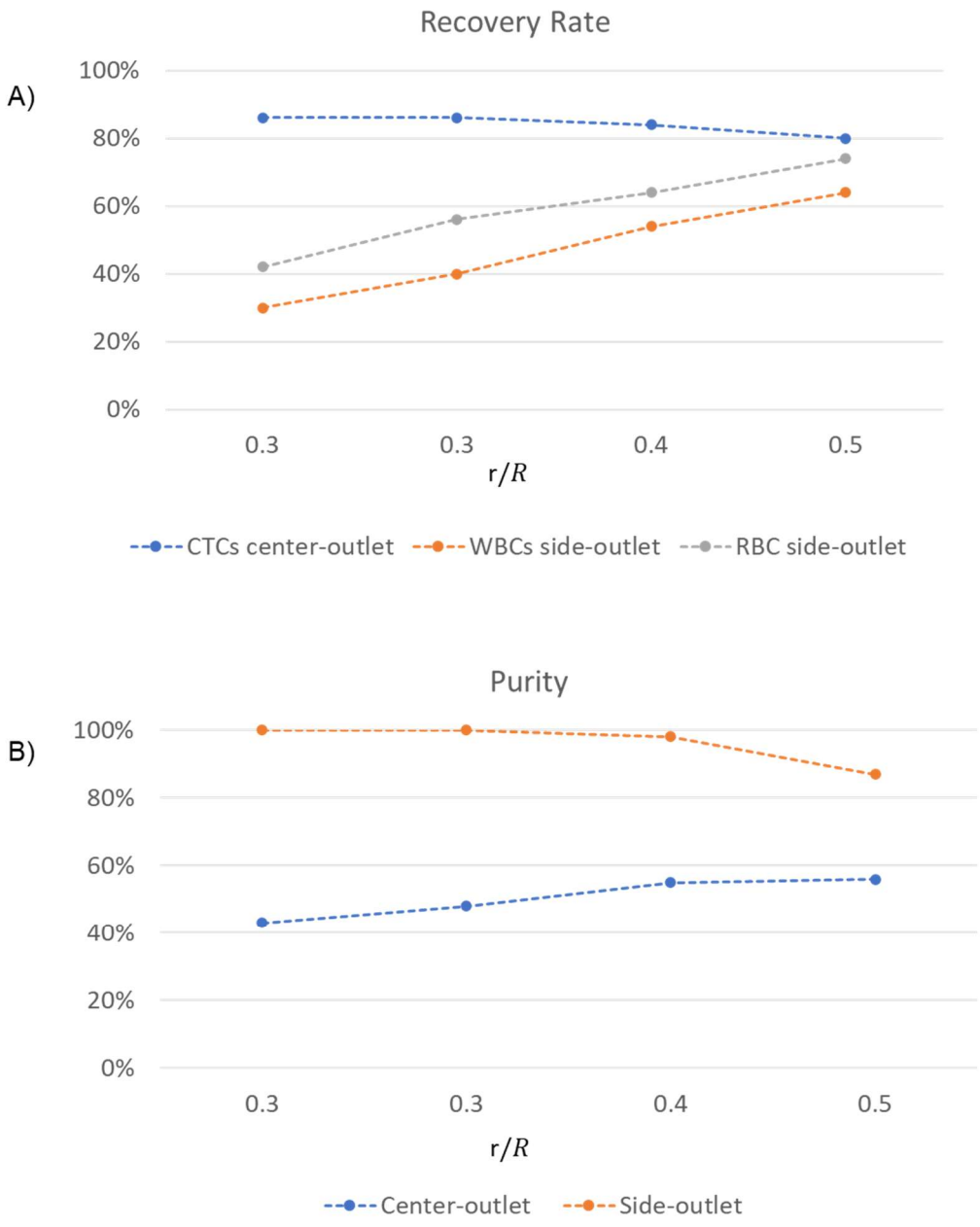

Figure 23 A) Recovery rate for CTCs, WBCs and RBCs at different distances from the axis of rotation B) Purity at the outlets at different distances from the axis of rotation

5.2.4 IDT position

Figure 24 presents the recovery rate of CTCs, WBCs and RBCs at different dimensionless IDTs-channel distance. d_{IDT} refers to the distance of each IDT to the channel, and it is transformed to a dimensionless value by dividing it with the width of the channel $W_{channel}$. The width of the channel used is $100\ \mu m$. The CTCs recovery rate and the blood cells purity at the side-outlets decrease when the distance IDTs-channel increases. This happens because the acoustic pressure generated on the channel decreases, so CTCs are not easily attracted to the pressure nodes and to the center-outlet. The highest CTCs recovery rate is obtained at 0.5. However, in order to also increase the recovery rate of RBCs and WBCs, the recommended dimensionless IDTs-channel distance would be 0.7, which in this case corresponds to a distance of $70\ \mu m$ from the $100\ \mu m$ channel.

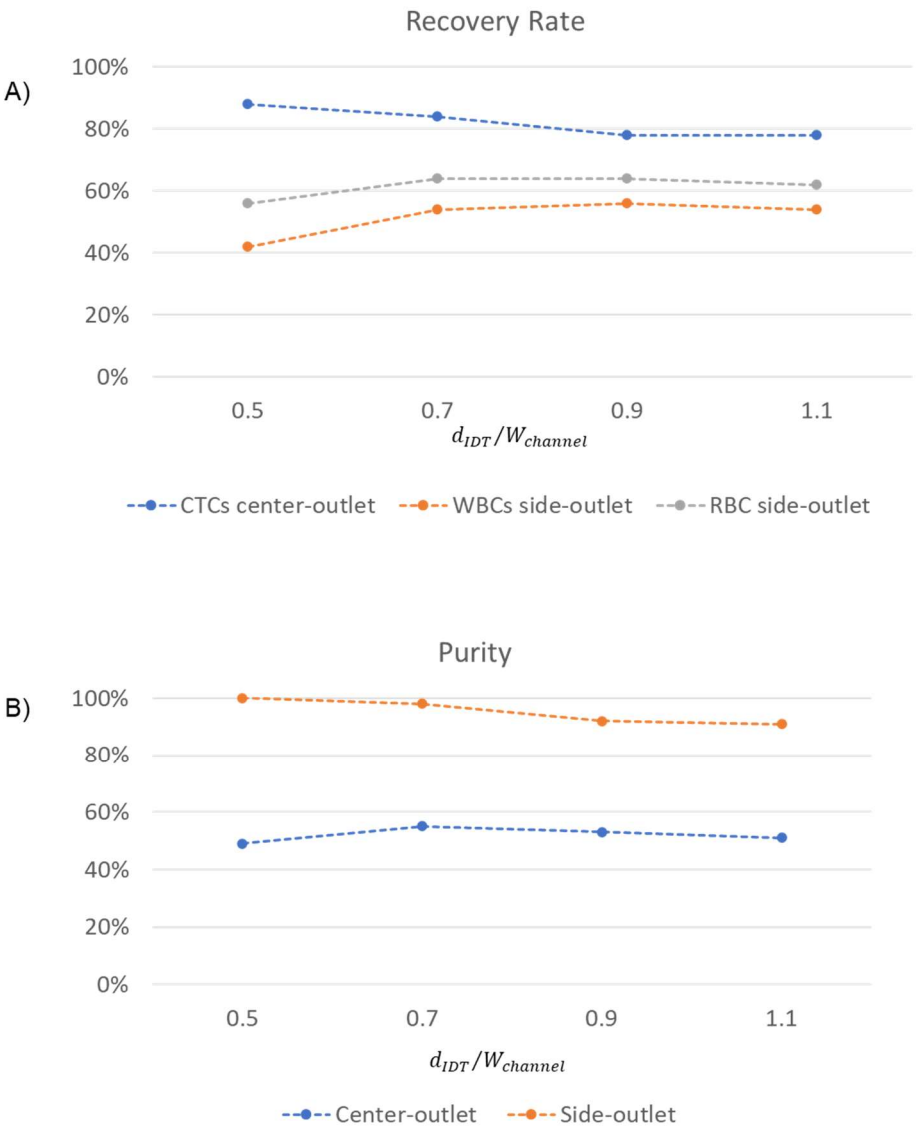

Figure 24 A) Recovery rate for CTCs, WBCs and RBCs with distance variation between IDTs and the channel. B) Purity at the outlets with distance variation between IDTs and the channel

5.2.5 Tilted angle of rotation

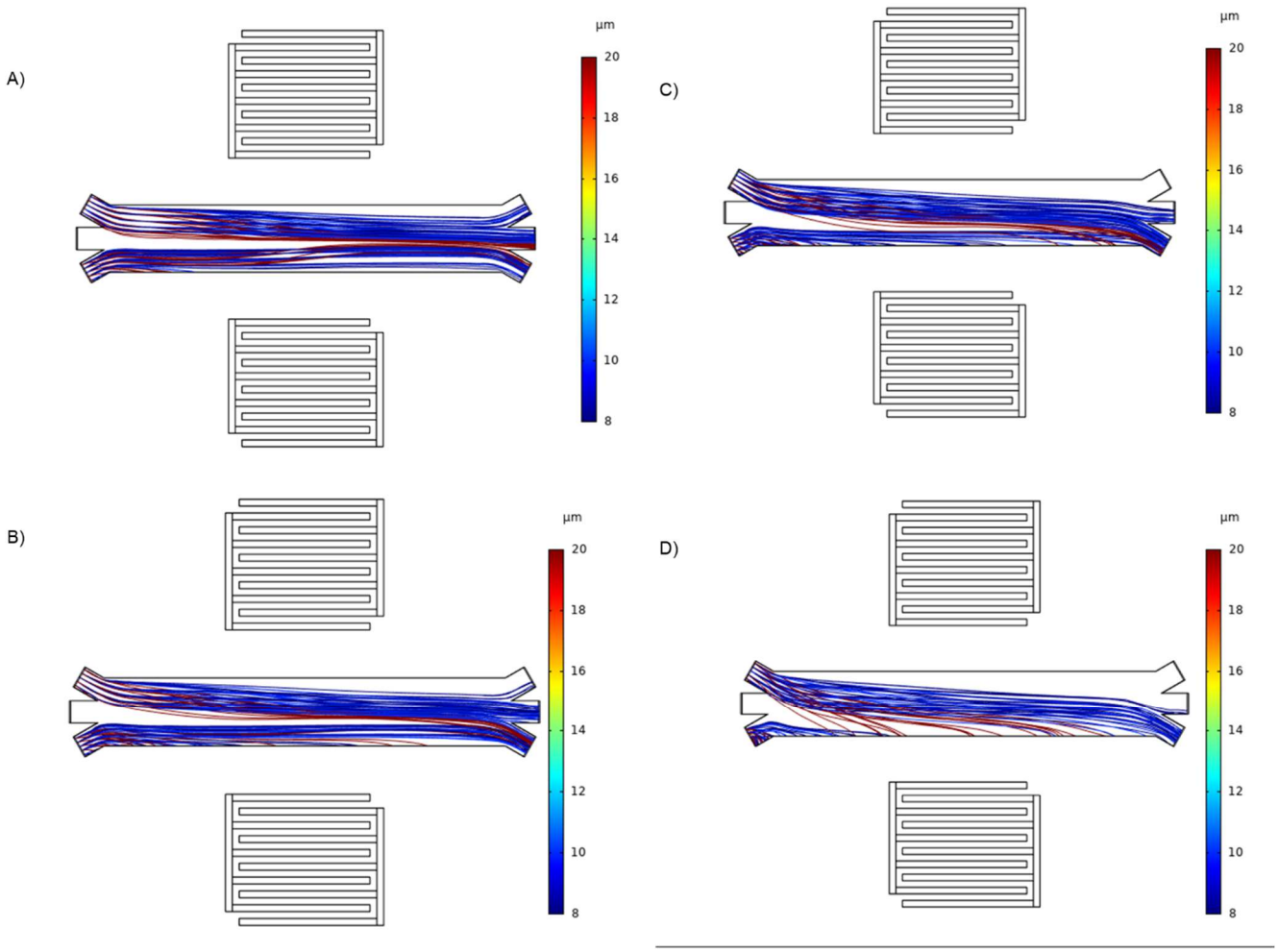

Figure 25 Path of CTCs in red color, WBCs and RBCs in blue color A) with a titled angle of 15º. B) with a tilted angle of 30º, C) with a tilted angle of 45º. D) with a tilted angle of 60º

Figure 25 shows the path of CTCs, WBCs and RBCs with a tilted angle of 15º, 30º, 45º and 60º. This means, the channel is no longer aligned radially to the disc. It can be seen the separation does not take place, since CTCs are not collected at the center-outlet, neither blood components at the sided outlets. This occurred because the centrifugal force changed the particles flow and acoustic force is no longer dominant, especially when the angle increases. To take advantage of a tilted angle when using acoustophoresis, a different geometry configuration would be suggested, with only one sample inlet and two outlets; and a low tilted angle.

5.2.7 Proportion of particles

Because the concentration of CTCs on blood samples is usually extremely low, a study with different proportions of CTCs and blood cells was performed, 10 and 1000 respectively. The recovery rate of CTCs obtained was of 80%, which is very close to the 84% with equal proportions. The recovery rate of WBCs and RBCs are also very similar. This means, the number of particles does not affect the separation performance, which is expected because interaction between particles is neglected.

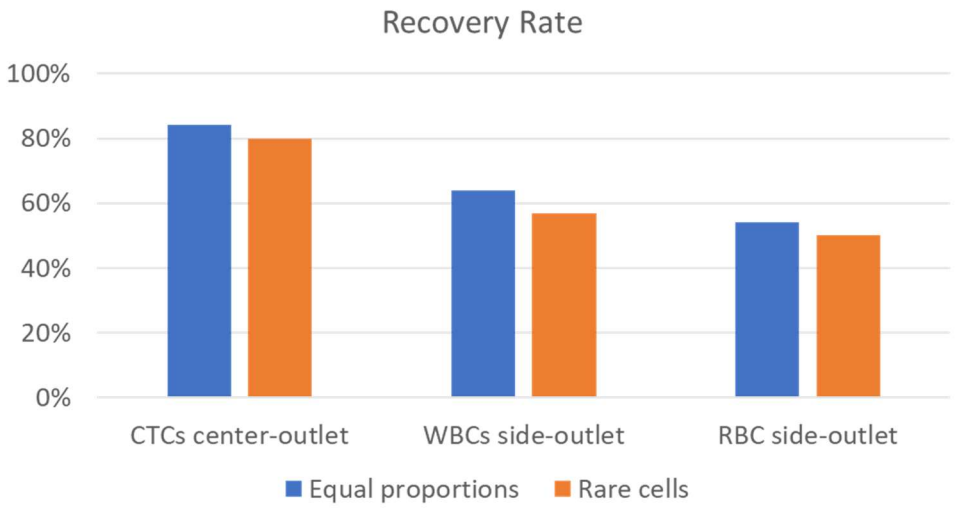

Figure 26 Recovery rate and purity of CTCs, WBCs, and RBCs with a 10:1000:1000 proportion

5.2.8 General discussion

In summary, the parametric study showed that the recovery rate of CTCs at the center-outlet decreases when:

- angular velocity increases, because particles stayed less time in the acoustic field, so they are not completely focused to the pressure nodes and the center-outlet.
- radius or distance to the axis of rotation increases, because angular velocity at the channel increases, and therefore previous point happens.

- distance between the IDTs and the channel increases, because the acoustic pressure generated on the channel decreases, so CTCs are not easily attracted to the pressure nodes.

Recovery rate of CTCs at the center-outlet increases when:

- voltage increases, because the acoustic pressure generated on the channel increases, so CTCs moved easier to the pressure node and to the center-outlet.

A general trend was observed between parametric curves of CTCs and other blood components. When recovery rate of CTCs increased, recovery rate of WBCs and RBCs decreases. This happened because an increase in CTCs recovery rate means this type of cell is more attracted to the pressure node. However, this behavior is also experienced by the other type of cells (WBCs and RBCS), in a lighter way they are also attracted to the pressure node, so less blood cells are collected on the sided-outlets and more of them are collected in the center inlet, which also means the purity of CTCs at the center inlet is decreased. In the other hand, when CTCs recovery rate decreases is because cells are not easily attracted to the pressure node at the center of the channel; but WBCs and RBCs are neither attracted to the pressure node, so they are easily collected on the sided outlets, increasing their recovery rate there and therefore increasing the CTCs purity at the center inlet.

In general, most of CTCs recovery rates were found between 70-90%, with purities at the sided outlets of 90-100%. The necessity of isolating and capturing CTCs for further analysis requires the highest recovery rate of CTCs at the center inlet, by trying to not lose them in the sided outlets. This value combined with the highest purity should be the ideal. However, other particle separation applications might be more interested in the highest purity possible at the center inlet, giving less importance to the recovery rate.

It was also found that when the channel is not aligned radially to the disc, separation does not take place in the geometry presented because the centrifugal force changed the particles direction and CTCs were not attracted to the pressure node located at the center of the channel. A different geometry configuration would be suggested in order to take advantage of a titled angle.

The recommended parameter values of the given geometry are a dimensionless angular velocity of 1.25. which in this case corresponds to 50 rad/s. A voltage of 1.15, which corresponds to 15V. A dimensionless channel-axis of rotation distance of 0.4, which corresponds to 2.5cm. A dimensionless IDTs-channel distance of 0.7, which corresponds to 70 μm from the 100 μm channel.

5.3 Comparison with non-centrifugal device SAWs-based platform

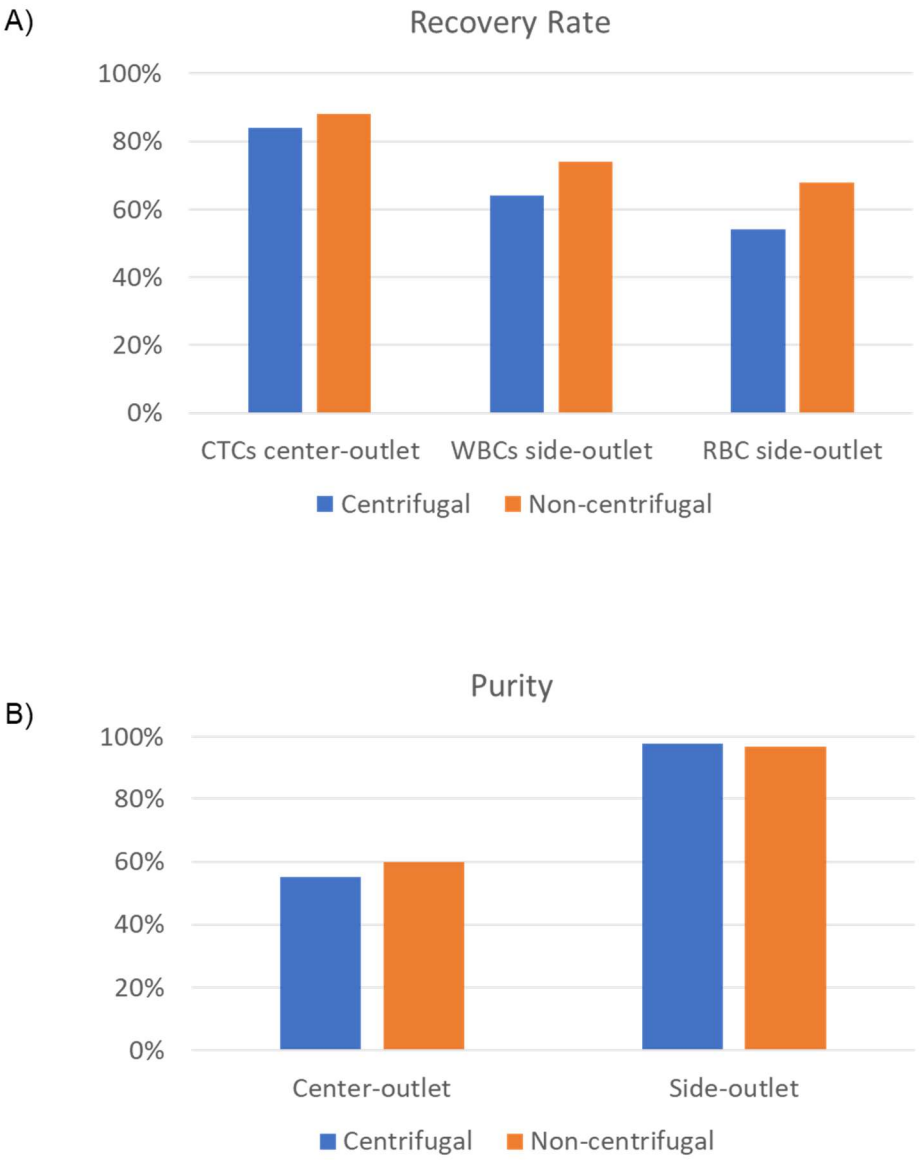

Figure 27 Comparison between centrifugal and non-centrifugal devices for cell separation A) Recovery rate B) Purity

The recovery rate and purity of a non-centrifugal device was obtained and compared to the results of the centrifugal device. The non-centrifugal platform took an inflow velocity of 8.3 mm/s in the center inlet, 7.83 mm/s in the upper side inlet, and 7.9 mm/s in the lower side inlet in order to have the same average velocity at the channel than the centrifugal platform rotating at 50 rad/s.

The purity of WBCs and RBCs at the side-outlets are almost equal in both configurations. The recovery rate of particles with centrifugal platform is slightly lower than on a non-centrifugal platform, and a larger difference is seen with RBCs and WBCs. This means, non-centrifugal devices focus slightly better CTCs to the pressure nodes at the center line of the channel and other blood cells to the sides. This can be explained because even though WBCs and RBCs are smaller in size in comparison to CTCs, they are larger in density; and density of particles takes an important role in centrifugal platforms.

5.3.1 Particle density

The sensibility of the device to particle density was obtained and compared between the centrifugal and non-centrifugal platform. Figure 28 shows the path of particles with 15 µm in diameter and densities of 1050-1170 kg/m^3 on both devices. The color bar indicates the variation of density. On the centrifugal device, particles with larger densities go the center-outlet and particles with smaller densities go to the side-outlets, however, on the non-centrifugal device all of them go to the center-outlet and are not separated. This means, centrifugal platforms for particle separation through acoustophoresis are more sensitive to density variations than non-centrifugal platforms, which can be explained by the centrifugal forces acting on the particles.

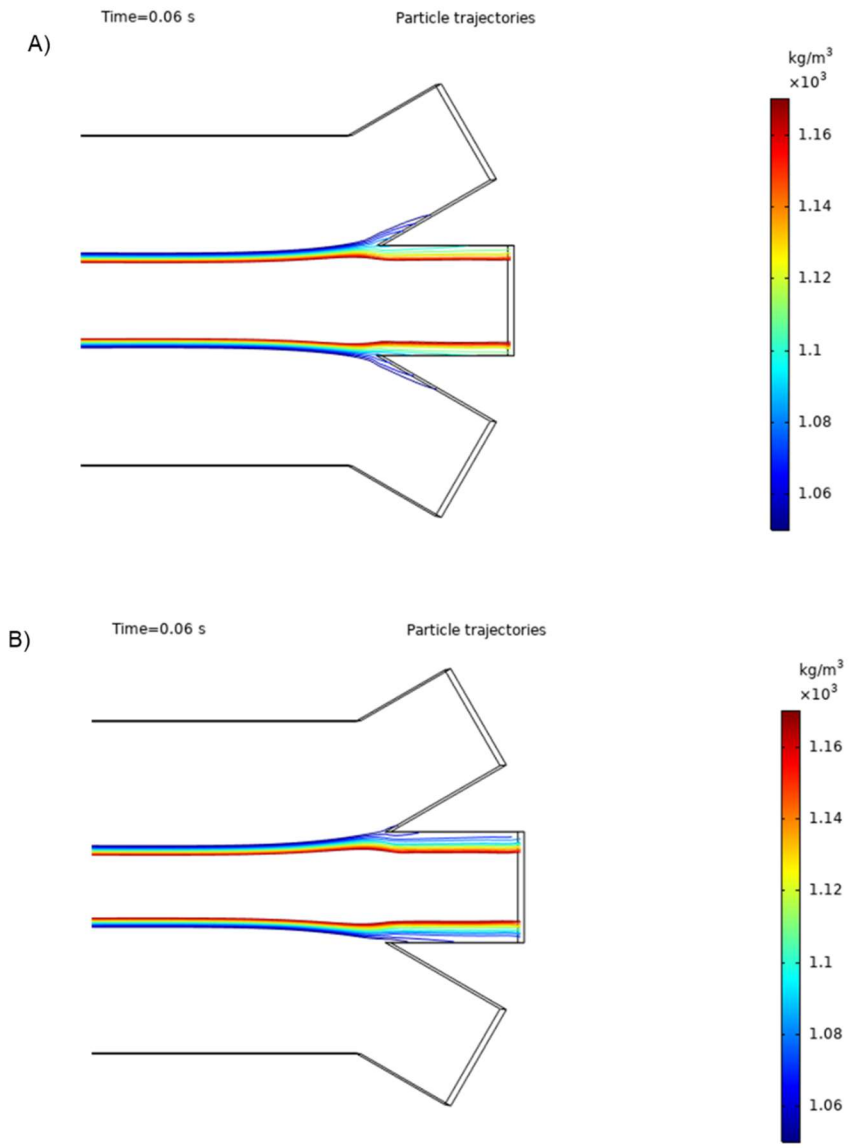

Figure 28 Particle path at the outlets of particles of equal size but different densities A) in a centrifugal device B) in a non-centrifugal device

5.4 Model validation BAWs-based platform

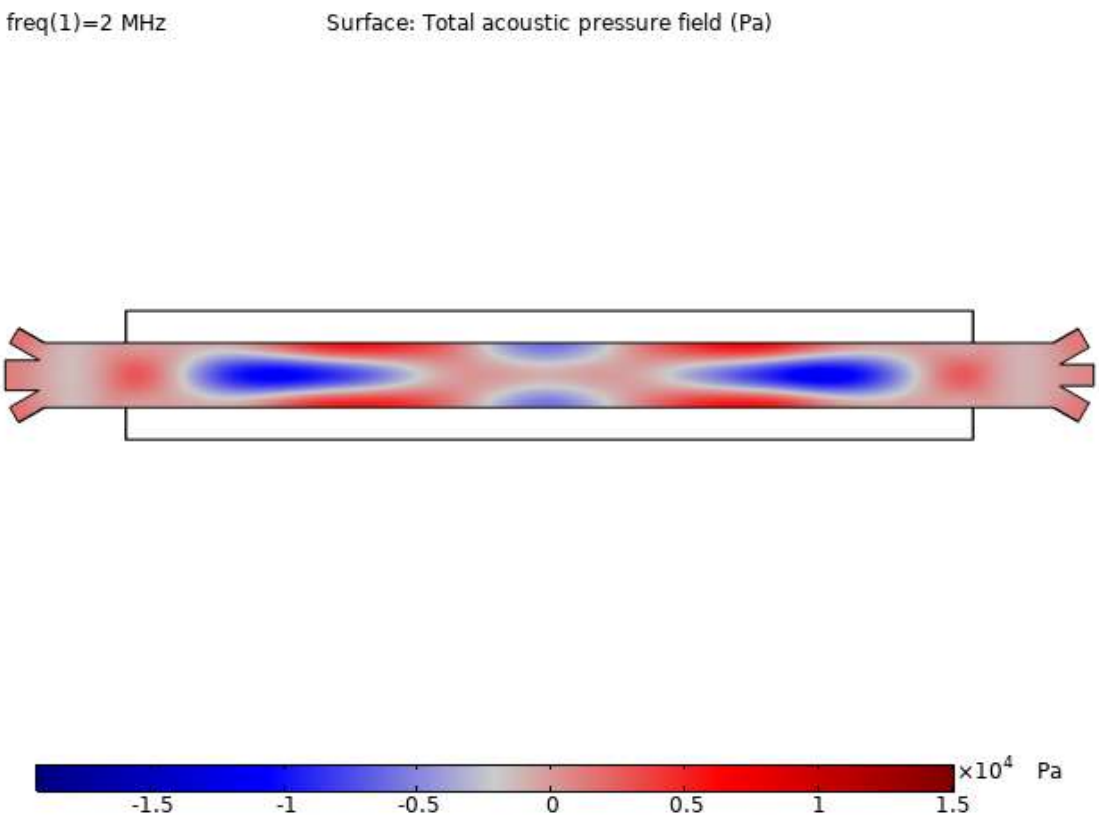

Figure 29 Acoustic pressure field of the model validation based on Dykes et al. work

An attempt to simulate the experimental work performed by Dykes et al. for platelets and WBCs separation in a BAWs-based microfluidic device was done. Figure 29 shows the acoustic pressure field generated. It is seen that it is not correct since the pressure node is not generated at the center of the channel as expected.

The way in which the correct pressure field was achieved was by adding a normal displacement 0f 0.8 µm to two parallel sides of the piezoelectric substrate. Figure 29A shows how the pressure node is generated at the middle of the channel with this modification, allowing the particle movement through the length of the channel and the separation of particles with different sizes at the outlets. Figure 29B shows the particles path of platelets and WBCs. As the experimental work, the sample entered by the sided inlets, and larger particles (WBCs) were moved to the centerline of the channel due to the

pressure node. Smaller particles (platelets) stayed next to the walls and were collected by the sided outlets.

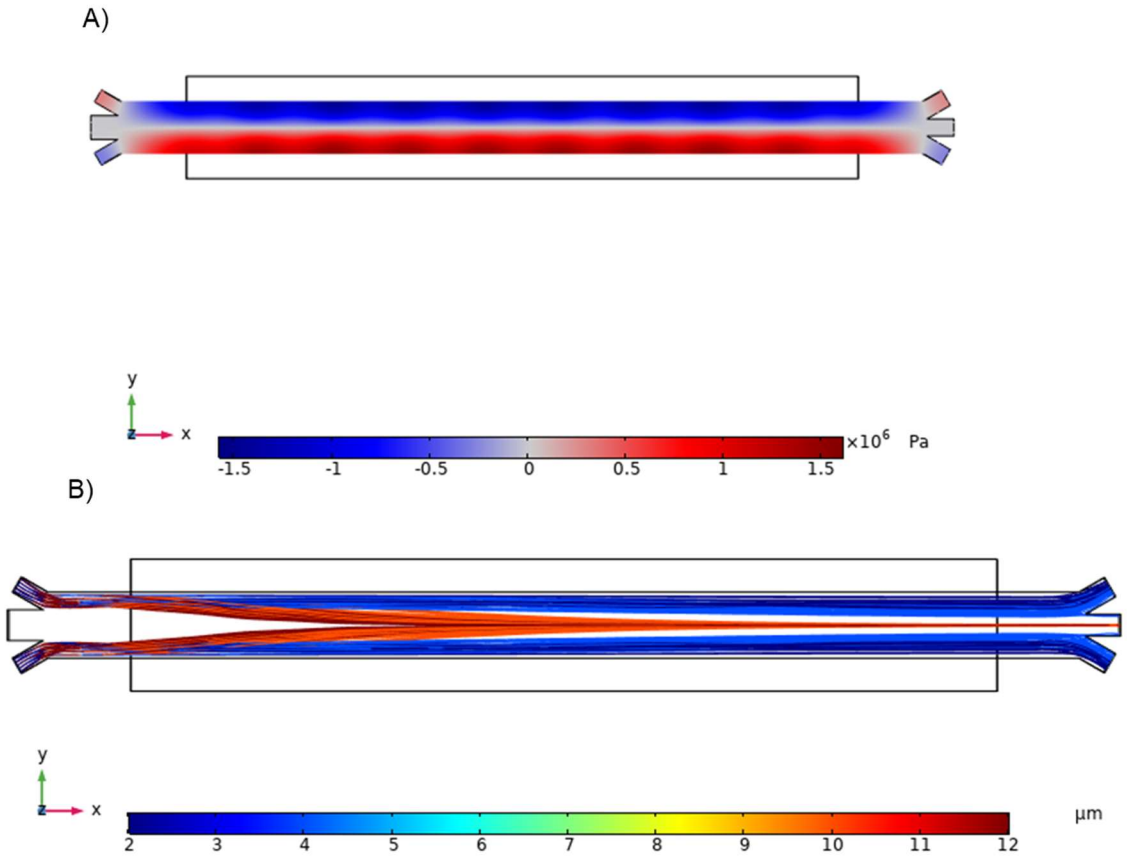

Figure 30 Modified model validation based on Dykes et al. work. A) Acoustic pressure field B) Particles path of platelets in blue and of WBCs in red

However, the model is not working correctly even when particle's separation is obtained. The acoustic pressure field should be generated because of the displacements of the piezoelectric material when an electric field is applied, a displacement should not be added as boundary condition. This means, in the model built, the acoustic pressure field is not generated by the voltage applied, it is generated because of the displacement added. This was verified when the intensity of the pressure field remained the same when modifying the voltage of the model, but changes when modifying the value of the displacement.

Chapter 6

This chapter presents a general conclusion of the thesis project and suggestions for future work.

6.1 Conclusions

Particle and cell separation is a powerful tool in clinical diagnostics and medical research since it is commonly the first stage for further analysis of individual components or for studying the effect of treatments on specific populations. It is also widely used for identification of diseases. CTCs separation is needed because they are believed to be the origin of cancer spread into other organs. Acoustophoresis in microfluidics is a technology with the potential of separating CTCs from blood samples, because the advantages of being label-free and highly sensitive. In the other hand, centrifugal microfluidics have the advantages of being portable and require a minimum amount of instrumentation. This work presented a computational study of acoustophoresis in centrifugal microfluidic platforms for particle and cell separation.

A 3D FEM-based model was built in COMSOL. First, the geometry consisted in a SAW-based device with 2 pairs of IDTs located on top of a piezoelectric substrate, with a rectangular fluid channel between the IDTs. By applying boundary conditions and input parameters, the model obtained the acoustic pressure in the channel. Then, the equations of fluid mechanics were solved to obtain the velocity field in the channel, considering centrifugal and Coriolis body forces. Finally, the particle's equation of motion was used to obtain the particles path, considering the centrifugal, Coriolis, drag, lift and acoustic radiation forces on the particle.

An attempt to validate the model with the experimental work performed by Shi et al. for particle separation in an acoustophoretic microfluidic device was done. However, it was not achieved since the acoustic pressure field was not generated correctly. A second attempt to validate the model was done with the simulation work performed by Shamloo. The pressure node was generated correctly at the center of the channel, which made

possible the particle separation. Larger particles moved to the center of the channel and collected by the center-outlet and smaller particles stayed next to the walls and collected by the side-outlets. The difference of this work is that the frequency applied was related to the width of the channel, and not the width of the IDTs as in the experimental work.

Based on Shamloo's work, a geometry was proposed for the acoustophoretic separation of CTCs from WBCs and RBCs. The geometry consisted of a rectangular channel with three inlets and three outlets placed on a $LiNbO_3$ substrate, between two pair of IDTs, with finger's width and spacing of 75 μm each. Solid sphere particles with diameters of 20 μm, 10 μm and 8 μm were considered for CTCs, WBCs and RBCs respectively, with densities of 1070 kg/m^3, 1080 kg/m^3, and 1110 kg/m^3. A parametric analysis was performed to study the influence of 5 parameters on the efficiency of the device. The efficiency was measured by the recovery rate of the three types of cells, and by the purity on each outlet.

The parametric study showed that the recovery rate of CTCs at the center-outlet decreases when the angular velocity increases, when the distance to the axis of rotation increases, and when the distance between the IDTs and the channel increases. Recovery rate of CTCs at the center-outlet increases when voltage increases.

A general trend was observed between parametric curves of CTCs and other blood components, when the recovery rate of CTCs increases, recovery rate of WBCs and RBCs decreases, and purity of CTCs at the center inlet also decreases. This also happened the other way around.

Additionally, it was found that when the channel was not aligned radially to the disc, separation did not take place. A different geometry configuration would be suggested to take advantage of a titled angle.

The study of different proportion of particles showed almost no effect on the separation performance, which was expected because interaction between particles was neglected in the model.

In general, most of CTCs recovery rates obtained were between 70-90%. Isolating CTCs for further analysis require the highest recovery rate of CTCs at the center inlet, by trying to not lose them in the sided outlets. However, other particle separation applications might

be more interested in the highest purity possible at the center inlet, giving less importance to the recovery rate.

A comparison of the centrifugal device with a non-centrifugal platform was performed. The purity of WBCs and RBCs at the side-outlets were almost equal in both configurations. The recovery rate of particles with centrifugal platform was slightly lower than on a non-centrifugal platform, due to the difference in density of the particles. The sensibility of the device to particle density variation was also compared between both devices, and centrifugal platforms were found to be more sensitive than non-centrifugal platforms, when the size of the particles is the same.

Because the validation of the SAWs-based platform with Shamloo's work applies a frequency related to the width of the channel, an attempt to simulate a BAWs-based platform was done. The validation of this model was performed with Dykes et al work. However, the pressure node was not generated at the center of the channel as expected. After a modification in the boundary conditions, a correct pressure field was achieved, and particles separated as in the experiments. However, the modification was an addition of normal displacement in two sides of the piezoelectric material, which meant that the acoustic pressure field is not generated by the voltage applied as it should, so future work in the model with this approach is needed.

Even if the model could not be correctly validated with experimental work, this project gives insights on the performance of a platform when joining acoustophoresis with centrifugal microfluidics. The parametric study gives an understanding on the behavior of the particles in the platform when some parameters are modified when the pressure field is generated correctly. This work might be used as the initial reference for future simulation studies of particle separation through acoustophoresis in centrifugal platforms and subsequently for experimental studies.

6.2 Future work

As future work, it is suggested to keep working on the simulation stage of the acoustic pressure field with both approaches, SAWs-based and BAWS-based platforms. For the SAWs-based model, the simulation should use the frequency value related with the IDTs width, as in experimental works. For BAWs-based model, the electric field should be applied correctly. A suggestion would be to add the channel's materials, such as PDMS, silicon or glass layers, with their respective boundary conditions. This might change the generation of the acoustic pressure field. After obtaining the pressure node as desired, other parameters can be modified to improve the recovery rate and purity of the separation, such as the voltage applied or the angular velocity as the parametric study presents previously. The model working correctly can be used to study the particle or cell separation for different applications, not necessarily cancer cells.

The second step suggested as future work would be the fabrication of the device. The difference between the SAWs-based platforms and BAWs-based platforms relies on how the acoustic pressure field is generated, on the materials of the devices and therefore on its fabrication.

The fabrication of SAWs-based platform consists in 2 sections, the fabrication of the microfluidic platform (Figure 28 B) and the fabrication of the acoustic system (Figure 28 A). For the fabrication of the platform, the standard method of the already published SAW devices consists of a mold replica and soft-lithography process forming the PDMS channel. The fabrication of the acoustic system consists of metal deposition and then lift-off photolithography process over the piezoelectric substrate. A union of the two parts through plasma bonding is required.

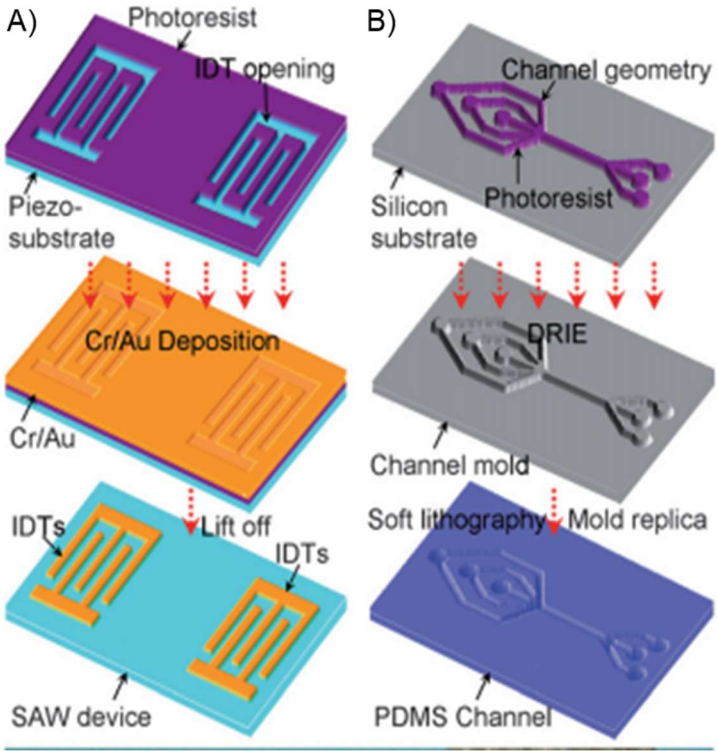

Figure 31 Schematic of the fabrication process of SAW microfluidic platform [29]

The BAWs-based platforms consist in a silicon channel made by anisotropic wet etching using Potassium hydroxide (KOH), and a piece of Pyrex glass anodically bonded to the top of the channel. The piezoceramic transducer is glued at the backside of the channel.

After the fabrication step of either of the platforms, testing would be required for measuring the performance of the device. Testing with polystyrene particles would be first recommended, and then with cancer cells. A configuration for applying voltage to platform while the platform is rotating needs to be developed.

After the proof of concept of acoustophoresis in centrifugal platforms, more stages on could be added to the platform for improving the recovery rate or for a complete analysis within it.

Appendix A

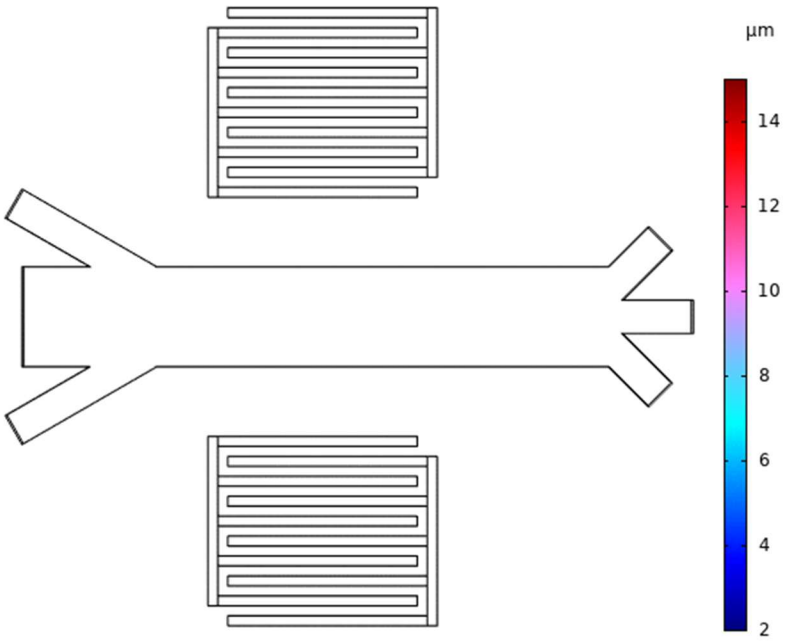

Figure 32 Video of the 3D model validation using Shamloo's work

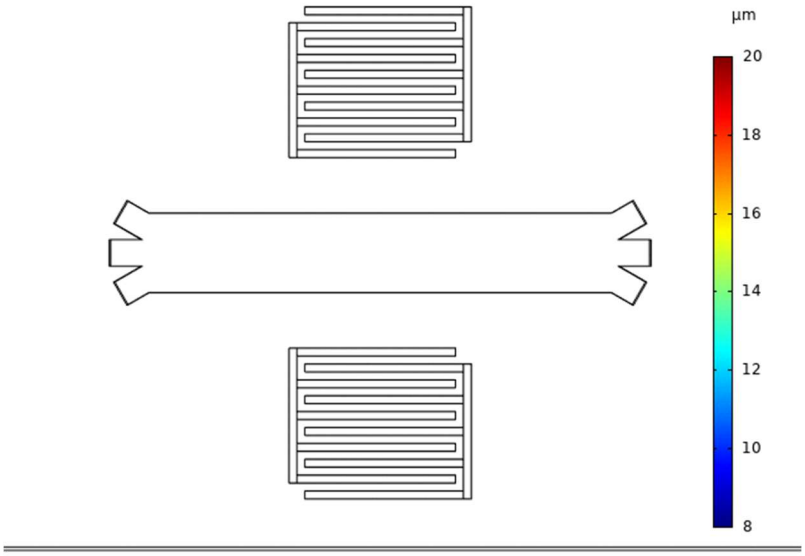

Figure 33 Video of the particles path of CTCs (in red) separation from WBCs and RBCs (in blue)

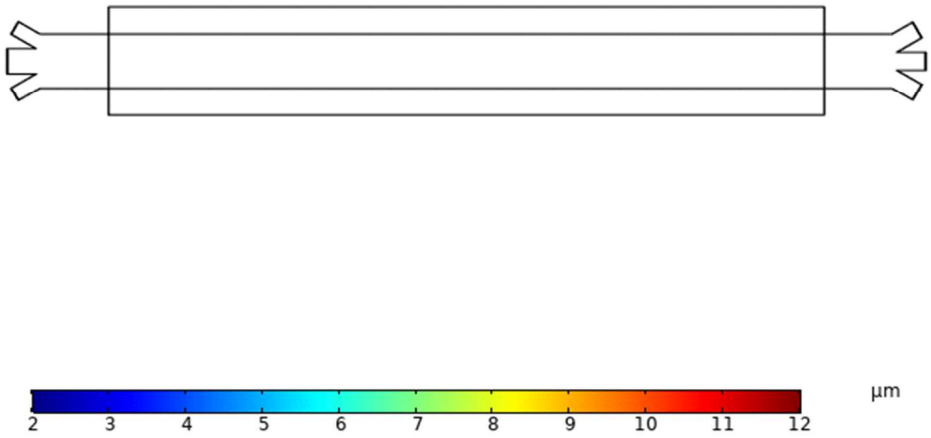

Figure 34 Video of the 3D model validation using Dyke's work

Bibliography

1. P. Sajeesh and A. K. Sen, “Particle separation and sorting in microfluidic devices: a review,” Microfluidics and Nanofluidics, vol. 17, no. 1, pp. 1–52, 2013.
2. M. J. Tomlinson, S. Tomlinson, X. B. Yang, and J. Kirkham, “Cell separation: Terminology and practical considerations,” Journal of Tissue Engineering, vol. 4, p. 204173141247269, 2012.
3. STEMCELL Technologies “Cell Separation Techniques”, 2021.
4. E. L. Jackson and H. Lu, “Advances in microfluidic cell separation and manipulation,” Current Opinion in Chemical Engineering, vol. 2, no. 4, pp. 398–404, 2013.
5. Y. Chen, P. Li, P.-H. Huang, Y. Xie, J. D. Mai, L. Wang, N.-T. Nguyen, and T. J. Huang, “Rare cell isolation and analysis in microfluidics,” Lab Chip, vol. 14, pp. 626–645, 2014.
6. J. Zhang, K. Chen, and Z. H. Fan, “Circulating Tumor Cell Isolation and Analysis,” *Advances in Clinical Chemistry*, pp. 1–31, 2016.
7. World Health Organization. “Cancer,”. 2021.
8. M. Wu, P.-H. Huang, R. Zhang, Z. Mao, C. Chen, G. Kemeny, P. Li, A. V. Lee, R. Gyanchandani, A. J. Armstrong, M. Dao, S. Suresh, and T. J. Huang, “Circulating tumor cell phenotyping via high-throughput acoustic separation,” Small, vol. 14, no. 32, p. 1801131, 2018.
9. A. Farahinia, W. J. Zhang, and I. Badea, “Novel microfluidic approaches to circulating tumor cell separation and sorting of blood cells: A review,” Journal of Science: Advanced Materials and Devices, 2021.
10. M. Antfolk, C. Magnusson, P. Augustsson, H. Lilja, and T. Laurell, “Acoustofluidic, label-free separation and simultaneous concentration of rare tumor cells from white blood cells,” Analytical Chemistry, vol. 87, no. 18, pp. 9322–9328, 2015. PMID: 26309066.
11. Z. Shen, A. Wu, and X. Chen, “Current detection technologies for circulating tumor cells,” *Chemical Society Reviews*, vol. 46, no. 8, pp. 2038–2056, 2017.

12. M. T. Gabriel, L. R. Calleja, A. Chalopin, B. Ory, and D. Heymann, “Circulating Tumor Cells: A Review of Non–EpCAM-Based Approaches for Cell Enrichment and Isolation,” Clinical Chemistry, vol. 62, no. 4, pp. 571–581, 2016.
13. J. Zhang, K. Chen, and Z. H. Fan, “Circulating Tumor Cell Isolation and Analysis,” Advances in Clinical Chemistry, pp. 1–31, 2016.
14. P. Bankó, S. Y. Lee, V. Nagygyörgy, M. Zrínyi, C. H. Chae, D. H. Cho, and A. Telekes, “Technologies for circulating tumor cell separation from whole blood,” Journal of Hematology & Oncology, vol. 12, no. 1, 2019.
15. Z. Dan and C. Daxiang, “Advances in isolation and detection of circulating tumor cells based on microfluidics,” Cancer Biology & Medicine, vol. 15, no. 4, p. 335, 2018.
16. M. Wu, A. Ozcelik, J. Rufo, Z. Wang, R. Fang, and T. Huang, “Acoustofluidic separation of cells and particles,” Microsystems Nanoengineering, vol. 5, 12 2019.
17. Lenshof A., Laurell T. Acoustophoresis. In: Bhushan B. (eds) Encyclopedia of Nanotechnology. Springer, Dordrecht. 2015.
18. N. Norouzi, H. C. Bhakta, and W. H. Grover, “Sorting cells by their density,” *PLOS ONE*, vol. 12, no. 7, 2017.
19. M. Diez-Silva, M. Dao, J. Han, C.-T. Lim, and S. Suresh, “Shape and Biomechanical Characteristics of Human Red Blood Cells in Health and Disease,” MRS Bulletin, vol. 35, no. 5, pp. 382–388, 2010.
20. J. Zhou, A. Kulasinghe, A. Bogseth, K. O’Byrne, C. Punyadeera, and I. Papautsky, “Isolation of circulating tumor cells in non-small-cell-lung-cancer patients using a multi-flow microfluidic channel,” Microsystems & Nanoengineering, vol. 5, no. 1, 2019.
21. R. Gorkin, J. Park, J. Siegrist, M. Amasia, B. S. Lee, J.-M. Park, J. Kim, H. Kim, M. Madou, and Y.-K. Cho, “Centrifugal microfluidics for biomedical applications,” Lab Chip, vol. 10, pp. 1758–1773, 2010.
22. R. Burger, D. Kirby, M. Glynn, C. Nwankire, M. O'Sullivan, J. Siegrist, D. Kinahan, G. Aguirre, G. Kijanka, R. A. Gorkin, and J. Ducrée, “Centrifugal microfluidics for cell analysis,” Current Opinion in Chemical Biology, vol. 16, no. 3-4, pp. 409–414, 2012.

23. J. Gilmore, M. Islam, and R. Martinez-Duarte, “Challenges in the use of compact disc-based centrifugal microfluidics for healthcare diagnostics at the extreme point of care,” Micromachines, vol. 7, no. 4, 2016.
24. B.P. Ho and L.G. Leal, “Inertial migration of rigid spheres in two-dimensional unidirectional flows”, J. Fluid Mech. 65, no. 02 (1974), pp. 365–400.
25. A. A. Bhagat, H. Bow, H. W. Hou, S. J. Tan, J. Han, and C. T. Lim, “Microfluidics for cell separation,” Medical & Biological Engineering & Computing, vol. 48, no. 10, pp. 999–1014, 2010.
26. J. Dykes, A. Lenshof, I.-B. Åstrand-Grundström, T. Laurell, and S. Scheding, “Efficient Removal of Platelets from Peripheral Blood Progenitor Cell Products Using a Novel Micro-Chip Based Acoustophoretic Platform,” PLoS ONE, vol. 6, no. 8, 2011.
27. P. Augustsson, C. Magnusson, M. Nordin, H. Lilja, and T. Laurell, “Microfluidic, Label-Free Enrichment of Prostate Cancer Cells in Blood Based on Acoustophoresis,” Analytical Chemistry, vol. 84, no. 18, pp. 7954–7962, 2012.
28. F. Olm, A. Urbansky, J. H. Dykes, T. Laurell, and S. Scheding, “Label-free neuroblastoma cell separation from hematopoietic progenitor cell products using acoustophoresis - towards cell processing of complex biological samples,” Scientific Reports, vol. 9, no. 1, 2019.
29. J. Shi, H. Huang, Z. Stratton, Y. Huang, and T. J. Huang, “Continuous particle separation in a microfluidic channel Via standing surface acoustic Waves (ssaw),” Lab on a Chip, vol. 9, no. 23, p. 3354, 2009.
30. J. Nam, Y. Lee, and S. Shin, “Size-dependent microparticles separation through standing surface acoustic waves,” Microfluidics and Nanofluidics, vol. 11, no. 3, pp. 317–326, 2011.
31. J. Nam, H. Lim, C. Kim, J. Yoon Kang, and S. Shin, “Density-dependent separation of encapsulated cells in a microfluidic channel by using a standing surface acoustic wave,” Biomicrofluidics, vol. 6, no. 2, p. 024120, 2012.
32. Y. Ai, C. K. Sanders, and B. L. Marrone, “Separation of Escherichia coli Bacteria from Peripheral Blood Mononuclear Cells Using Standing Surface Acoustic Waves,” Analytical Chemistry, vol. 85, no. 19, pp. 9126–9134, 2013.

33. X. Ding, Z. Peng, S.-C. S. Lin, M. Geri, S. Li, P. Li, Y. Chen, M. Dao, S. Suresh, and T. J. Huang, “Cell separation using tilted-angle standing surface acoustic waves,” Proceedings of the National Academy of Sciences, vol. 111, no. 36, pp. 12992–12997, 2014.
34. P. Li, Z. Mao, Z. Peng, L. Zhou, Y. Chen, P.-H. Huang, C. I. Truica, J. J. Drabick, W. S. El-Deiry, M. Dao, S. Suresh, and T. J. Huang, “Acoustic separation of circulating tumor cells,” Proceedings of the National Academy of Sciences, vol. 112, no. 16, pp. 4970–4975, 2015.
35. M. Wu, P.-H. Huang, R. Zhang, Z. Mao, C. Chen, G. Kemeny, P. Li, A. V. Lee, R. Gyanchandani, A. J. Armstrong, M. Dao, S. Suresh, and T. J. Huang, “Circulating Tumor Cell Phenotyping via High-Throughput Acoustic Separation,” Small, vol. 14, no. 32, p. 1801131, 2018.
36. K. Wang, W. Zhou, Z. Lin, F. Cai, F. Li, J. Wu, L. Meng, L. Niu, and H. Zheng, “Sorting of tumour cells in a microfluidic device by multi-stage surface acoustic waves,” Sensors and Actuators B: Chemical, vol. 258, pp. 1174–1183, 2018.
37. H. Bruus, “Acoustofluidics 1: Governing equations in microfluidics,” Lab Chip, vol. 11, pp. 3742–3751, 2011.
38. B. Yılmaz and F. Yılmaz, “Lab-on-a-Chip Technology and Its Applications,” Omics Technologies and Bio-Engineering, pp. 145–153, 2018.
39. H. O. Fatoyinbo, “Microfluidic devices for cell manipulation,” Microfluidic Devices for Biomedical Applications, pp. 283–350, 2013.
40. M. Madadelahi, L. F. Acosta-Soto, S. Hosseini, S. O. Martinez-Chapa, and M. J. Madou, “Mathematical modeling and computational analysis of centrifugal microfluidic platforms: a review,” Lab on a Chip, vol. 20, no. 8, pp. 1318–1357, 2020.
41. D. C. Duffy, H. L. Gillis, J. Lin, N. F. Sheppard, and G. J. Kellogg, “Microfabricated centrifugal microfluidic systems: Characterization and multiple enzymatic assays,” Analytical Chemistry, vol. 71, no. 20, pp. 4669–4678, 1999.
42. O. Strohmeier, M. Keller, F. Schwemmer, S. Zehnle, D. Mark, F. von Stetten, R. Zengerle, and N. Paust, “Centrifugal microfluidic platforms: advanced unit

operations and applications," Chemical Society Reviews, vol. 44, no. 17, pp. 6187–6229, 2015.

43. R. Nasiri, A. Shamloo, J. Akbari, P. Tebon, M. R. Dokmeci, and S. Ahadian, "Design and Simulation of an Integrated Centrifugal Microfluidic Device for CTCs Separation and Cell Lysis," Micromachines, vol. 11, no. 7, p. 699, 2020.
44. J. Zhang, S. Yan, D. Yuan, G. Alici, N.-T. Nguyen, M. Ebrahimi Warkiani, and W. Li, "Fundamentals and applications of inertial microfluidics: a review," Lab on a Chip, vol. 16, no. 1, pp. 10–34, 2016.
45. J. M. Martel and M. Toner, "Inertial Focusing in Microfluidics," Annual Review of Biomedical Engineering, vol. 16, no. 1, pp. 371–396, 2014.
46. A. Lenshof, M. Evander, T. Laurell, and J. Nilsson, "Acoustofluidics 5: Building microfluidic acoustic resonators," Lab Chip, vol. 12, pp. 684–695, 2012.
47. F. Petersson, L. berg, A.-M. Swrd-Nilsson, and T. Laurell, "Free flow acoustophoresis: microfluidic-based mode of particle and cell separation," Analytical Chemistry, vol. 79, no. 14, pp. 5117–5123, 2007. PMID: 17569501.
48. G. Destgeer and H. J. Sung, "Recent advances in microfluidic actuation and micro-object manipulation via surface acoustic waves," Lab Chip, vol. 15, pp. 2722–2738, 2015.
49. M. Gedge and M. Hill, "Acoustofluidics 17: Theory and applications of surface acoustic wave devices for particle manipulation," Lab on a chip, vol. 12, pp. 2998–3007, 07 2012.
50. H. Bruus, "Acoustofluidics 7: The acoustic radiation force on small particles," Lab on a Chip, vol. 12, no. 6, p. 1014, 2012.
51. M. Settnes and H. Bruus, "Forces acting on a small particle in an acoustical field in a viscous fluid," Physical Review E, vol. 85, no. 1, 2012.
52. J. Shi, X. Mao, D. Ahmed, A. Colletti, and T. J. Huang, "Focusing microparticles in a microfluidic channel with standing surface acoustic waves (SSAW)," Lab Chip, vol. 8, no. 2, pp. 221–223, 2008.
53. J. Dual and D. Möller, "Acoustofluidics 4: Piezoelectricity and application in the excitation of acoustic fields for ultrasonic particle manipulation," Lab on a Chip, vol. 12, no. 3, p. 506, 2012.

54. A. Shamloo and M. Boodaghi, “Design and simulation of a microfluidic device for acoustic cell separation,” Ultrasonics, vol. 84, pp. 234–243, 2018.
55. A. Shamloo and F. Y. Parast, “Simulation of Blood Particle Separation in a Trapezoidal Microfluidic Device by Acoustic Force,” IEEE Transactions on Electron Devices, vol. 66, no. 3, pp. 1495–1503, 2019.
56. J. Zhang, K. Chen, and Z. H. Fan, “Circulating Tumor Cell Isolation and Analysis,” Advances in Clinical Chemistry, pp. 1–31, 2016.
57. H. Bruus, “Acoustofluidics 2: Perturbation theory and ultrasound resonance modes,” Lab Chip, vol. 12, no. 1, pp. 20–28, 2012.
58. COMSOL Multiphysics® v. 5.6. Materials Library.
59. MEGGITT. Ferroperm Piezoceramics. Data for modelling. https://www.meggittferroperm.com/resources/data-for-modelling/